3-D uncertainty-based topographic change detection with structure-from-motion photogrammetry: precision maps for ground control and directly georeferenced surveys

James, M. R.[a], Robson, S.[b] and Smith, M. W.[c]

[a] Lancaster Environment Centre, Lancaster University, Lancaster, LA1 4YQ, U.K. (corresponding author: m.james@lancs.ac.uk, +44 (0)1524 593571)

[b] Department of Civil, Environmental and Geomatic Engineering, University College London, Gower Street, London, WC1E 6BT, U.K.

[c] School of Geography, University of Leeds, Leeds, LS2 9JT, U.K.

Short title: *3-D uncertainty-based change detection for SfM surveys*

Abstract

Structure-from-motion (SfM) photogrammetry is revolutionising the collection of detailed topographic data, but insight into geomorphological processes is currently restricted by our limited understanding of SfM survey uncertainties. Here, we present an approach that, for the first time, specifically accounts for the spatially variable precision inherent to photo-based surveys, and enables confidence-bounded quantification of 3-D topographic change. The method uses novel 3-D precision maps that describe the 3-D photogrammetric and georeferencing uncertainty, and determines change through an adapted state-of-the-art fully 3-D point-cloud comparison (M3C2; Lague*, et al.*, 2013), which is particularly valuable for complex topography. We introduce this method by: (1) using simulated UAV surveys, processed in photogrammetric software, to illustrate the spatial variability of precision and the relative influences of photogrammetric (e.g. image network geometry, tie point quality) and georeferencing (e.g. control measurement) considerations; (2) we then present a new Monte Carlo procedure for deriving this information using standard SfM software and integrate it into confidence-bounded change detection; before (3) demonstrating geomorphological application in which we use benchmark TLS data for validation and then estimate sediment budgets through differencing annual SfM surveys of an eroding badland. We show how 3-D precision maps enable more probable erosion patterns to be identified than existing analyses, and how a similar overall survey precision could have been achieved with direct survey georeferencing for camera position data with precision half as good as the GCPs'. Where precision is limited by weak georeferencing (e.g. camera positions with multi-metre precision, such as from a consumer UAV), then overall survey precision can scale as $n^{-½}$ of the control precision (n = number of images). Our method also provides variance-covariance information for all parameters. Thus, we now open the door for SfM practitioners to use the comprehensive analyses that have underpinned rigorous photogrammetric approaches over the last half-century.

Keywords: precision maps, DEM uncertainty, structure-from-motion, georeferencing, UAV

Introduction

Detailed digital elevation models (DEMs) produced by high resolution topography (HiRT) measurement techniques are accelerating our understanding of geomorphological processes. Increasingly, digital photographs are being used to generate such topographic data (particularly from consumer cameras and unmanned aerial vehicles (UAVs)), supported by processing software based on structure from motion (SfM). Such techniques are being used to, for example, model fluvial processes and drive hydraulic models (Dietrich, 2016; Javernick*, et al.*, 2016; Woodget*, et al.*, 2015), reconstruct the propagation of glacial outburst floods (Westoby*, et al.*, 2015), understand wave run-up and coastal cliff erosion (Casella*, et al.*, 2014; James and Robson, 2012), quantify eroded soil and gully volumes (Castillo*, et al.*, 2012; Eltner*, et al.*, 2015; Gomez-Gutierrez*, et al.*, 2014), examine landslide and glacier movement (Lucieer*, et al.*, 2014; Ryan*, et al.*, 2015), characterise ice surface roughness to parameterise surface melt models (Smith*, et al.*, 2016) and determine the evolution of active lava flows and domes (James and Robson, 2014b; James and Varley, 2012). The flexibility of SfM-processing enables a wide range of imagery and imaging geometries to be used and is central to the widespread adoption of HiRT techniques. However, this flexibility can result in substantial variations in data quality, both between and, crucially, within surveys (Smith and Vericat, 2015), which is often poorly quantified. Here, we derive and demonstrate a novel approach to enable rigorous and confidence-bounded change detection in complex topography from photo-based surveys, based on precision maps which characterise the 3-D survey quality and its spatial variability. Whilst we focus on airborne surveys, the approach is of equal value for terrestrially-acquired data.

DEM uncertainty

Understanding survey uncertainties is critical for appropriate error propagation into downstream topographic analyses, and the importance of DEM uncertainty when deriving geomorphological parameters and associated process models has been widely demonstrated (e.g. Lallias-Tacon*, et al.*, 2014; Milan*, et al.*, 2011; Wheaton*, et al.*, 2010). When determining topographic change (e.g. for estimating sediment budgets), vertical uncertainty can be considered for conventional DEMs of difference (DoDs) to enable the significance of changes to be estimated (Brasington*, et al.*, 2003; Lane*, et al.*, 2003). Changes smaller than a specified 'level of detection' (LoD) can then be disregarded where, for two DEMs with vertical standard deviations of error, σ_{Z1} and σ_{Z2},

$$\mathrm{LoD} = t({\sigma_{Z1}}^2 + {\sigma_{Z2}}^2)^{½} \qquad 1),$$

and *t* is an appropriate value for the required confidence level. LoD values are typically calculated to represent a 95% confidence level (i.e. $\mathrm{LoD}_{95\%}$), for which, under the *t* distribution, *t* = 1·96.

Single LoD values for use across entire DoDs can be estimated from relatively standard error assessments such as the root mean square error (RMSE) on independently surveyed check points for the constituent DEMs (e.g. Milan*, et al.*, 2007). Although such RMSE values can provide valuable insight into overall survey performance, they do not expose the spatial variability that can be highly relevant for detailed DEM analyses (Chu*, et al.*, 2014; Gonga-Saholiariliva*, et al.*, 2011; Oksanen and Sarjakoski, 2006; Weng, 2002) and their use can result in issues such as significant volumes from small elevation changes over large areas being neglected (e.g. overbank deposition, Brasington*, et al.*, 2003). More challengingly, spatially variable LoD values can be determined, either manually, via classification from other information, or through using underlying data to estimate parameters such as subgrid roughness (Brasington, *et al.*, 2003; Lane, *et al.*, 2003; Wheaton, *et al.*, 2010). However, by disregarding horizontal error through conventional use of (2.5-D) DEMs, uncertainty estimates for topographic change detection (which include precision and accuracy components) can lose validity in regions of steep topography (Lague, *et al.*, 2013).

3-D analysis and photo-based surveys

Consequently, and to take full advantage of large and fully 3-D datasets such as from terrestrial laser scanners (TLSs), multiple methods for directly comparing point clouds have been derived (see Lague, *et al.* (2013) for a useful summary). One approach, Multiscale Model to Model Cloud Comparison (M3C2; Lague, *et al.*, 2013) is of particular use in geomorphology because it incorporates a confidence interval and thus provides 3-D analysis of topographic change constrained by spatially variable $LoD_{95\%}$ values, and is applicable in any type of terrain. Within the M3C2 algorithm, measurement precision is estimated from local surface roughness, which is highly appropriate for the TLS data for which it was primarily designed. However, the smoothing or filtering commonly incorporated into image matching algorithms (e.g. Furukawa and Ponce, 2007; Hirschmuller, 2008) can strongly mute the representation of small-scale roughness in photo-derived point clouds. Furthermore, the complex photogrammetric and georeferencing processes result in point coordinate precision being a function of survey characteristics such as image network geometry and the quality, quantity and distribution of control, leading to point position errors that are spatially variable but locally highly correlated (due to neighbouring points generally being derived from the same images and thus subject to similar error). Thus, purely roughness-based precision estimates are unlikely to be representative of uncertainty in photogrammetric point clouds.

As for all topographic measurement techniques, the georeferencing process is central to achieving data with suitable repeatability (i.e. good spatial precision) for detecting change and, for photo-based surveys, georeferencing is usually carried out by measuring ground control points (GCPs). However, the deployment and precise ground survey of GCP arrays can require considerable effort, as well as the availability of relatively expensive survey equipment (e.g. dGPS or total station), and this can offset the otherwise cost-effective combination of UAV and SfM-MVS processing. An alternative is 'direct georeferencing', in which control is provided through measurements of camera orientations only (e.g. Cramer*, et al.*, 2000; Förstner*, et al.*, 2013). By not requiring ground-based measurements, the direct approach has a critical advantage for aerial survey over hazardous terrain, and has been shown capable of measurement precisions of order 0·1 m for piloted SfM-based surveys with survey-grade GPS synchronised with image capture (Nolan and DesLauriers, 2016; Nolan*, et al.*, 2015). However, for most current consumer UAVs, precise directly georeferenced work is prevented by their use of low-quality, multi-metre precision, on board GPS (Carbonneau and Dietrich, 2016) but survey-grade GPS is being increasingly installed (e.g. Bláha*, et al.*, 2011; Chiang*, et al.*, 2012; Eling*, et al.*, 2015; Gabrlik, 2015; Hugenholtz*, et al.*, 2016; Mian*, et al.*, 2015; Rehak*, et al.*, 2013; Turner*, et al.*, 2014) and such systems are likely to develop into widespread, invaluable tools for geomorphological research. Consequently, understanding the differences in survey performance between using GCPs or direct georeferencing will be integral to optimising future survey strategies aimed at quantifying topography and topographic change.

Here, we have the overall aims of enabling uncertainty-bounded analysis of topographic change using SfM and exploring the implications of different georeferencing styles. Our approach is based on deriving maps of 3-D precision from the precision estimates that are integral to rigorous photogrammetric processing, and which capture the variation of both photogrammetric and georeferencing uncertainties across the full extent of surveys. Within the paper, we initially summarise how precision estimates are derived during photogrammetric processing and then (1), we introduce the insight that precision maps provide into spatial variability and sensitivity to survey and georeferencing parameters, using simulated UAV surveys processed with rigorous close-range photogrammetric software. Unfortunately, the current range of SfM-based software commonly used to process most geomorphological surveys does not yet offer detailed precision information. Thus (2), we implement a novel Monte Carlo approach that enables precision maps to be produced when using SfM-based software, and we integrate the resulting precision estimates with the M3C2 algorithm to enable confidence-bounded 3-D change measurement for photo-based surveys. Finally (3), we demonstrate our method on an eroding badlands catchment where erosion assessments over ~4,700 m^2 require sub-decimetre level precision (Smith and Vericat, 2015).

Photogrammetric precision estimates

Precision estimates are an integral component of rigorous photogrammetric processing and result from the optimisation procedures used when deriving 3-D information from photographs (Cooper and Robson, 1996; Förstner and Wrobel, 2013). Here, and throughout, we use ‘precision’ to refer to the expected one standard deviation of an estimated or measured value. Image processing comprises the automatic identification of ‘tie point’ features (often tens of thousands) in the images, matching them across multiple images, and making initial estimates of their 3-D point coordinates from the two-dimensional image observations. In geomorphological surveys, the tie points within this image network usually represent distinct features on the ground (such as, depending on image scale, grains, boulders, the edges of rills) and thus their positions map the topographic surface (Figure 1a). Subsequent photogrammetric processing is based on ‘bundle adjustment’, a least-squares global optimisation which minimises the total residual error on image observations by simultaneously adjusting camera parameters and orientations, and the 3-D point positions (Granshaw, 1980). Just as when applying a linear model to multiple measurements of two variables, the observational redundancy within the bundle adjustment (due to the large number of tie points) and the use of a least-squares approach enables precision estimates to be derived for all adjusted model parameters. These parameters include camera models and the 3-D point positions and, by also considering variances and covariances, correlations between camera parameters can be identified, and each tie point can be accompanied by a 3-D measurement precision ellipsoid (Figure 1a). The point precision estimates can be used to define the repeatability of measurements made within the results (e.g. relative distances between points), given the error associated with the input measurements (i.e. the tie point image observations). Our precision maps are based on the 3-D precision estimates made for the tie point coordinates, and are thus most effective for dense distributions of tie points.

Control measurements are included within an adjustment to introduce an external coordinate system in which the precision estimates are reported and the survey is georeferenced (Figure 1b). Typically, to ensure geometric coverage over the entire survey area, more control measurements are used than the minimum required to uniquely define the coordinate datum and, thus, the relative shape of the survey can also be influenced. Each control measurement (e.g. a dGPS ground survey measurement of a control point position, or a camera position) is characterised by a defined measurement precision that is included within the adjustment calculations; consequently, if control is only given to poor precision, then this propagates through to, and can dominate, the derived 3-D topographic point coordinate precision values (Figure 1c). In this case, although the overall precision of point locations within the external coordinate system is degraded by the poor control measurement precision, relative distances between points within the survey may remain precise (i.e. with the 'internal' precision of the survey controlled by the quality of the tie points, Figure 1a).

Another way of considering this is that the relative shape of the topographic surface derived internally within the photogrammetric network may be good, but its overall georeferencing to an external coordinate system (as defined by a best-fit Helmert transform, comprising scale, rotation and translation components (Förstner*, et al.*, 2013)) is weakly constrained. Thus, the final surface model precision can be separated into components of the external coordinate system georeference, and the shape of the model (e.g. Förstner*, et al.* (2013); a concept also used recently for DEM error (Carbonneau and Dietrich, 2016)). Through separating the georeference and the surface shape components of the precision estimates, insight can be gained into the relative contributions of control measurements and tie points – i.e. how important the control measurements are in influencing the shape of a survey as well as for overall georeferencing.

Within a photogrammetric workflow, precision estimation precedes, and is independent from, the dense image matching from which DEMs are ultimately derived. However, the dense matching process does not optimise any aspects of the image network and, therefore, does not affect the underlying precision estimates. Additional error can be introduced by the dense matching itself, but work on early stereo-matching algorithms (Lane*, et al.*, 2000) found this to be less important for resulting DEMs than issues such as the presence of vegetation and data resolution. With error from modern multi-image dense matching algorithms likely to be less than from early stereo-matchers, in this work, we consider that tie point precision can be used to represent the main measurement contribution to surface model precision.

Thus, in our approach, we ascribe precision values to the dense cloud points based on the precision of their underlying sparse tie points. Note that, because precision estimates are derived from the least-squares minimisation of image residuals, some systematic errors inherent in photogrammetric processing (such as doming deformation of the surface), which are not detectable in image residuals, are not included in the precision estimates. Such errors represent internal accuracy problems that can be identified by using check points (Chandler, 1999), and have to be mitigated by the use of suitably precise and well-distributed control, an accurate camera model or appropriately strong imaging geometries (James and Robson, 2014a; Wackrow and Chandler, 2011). Thus, care needs to be taken to avoid interpreting precision maps as a guarantee of accuracy, which can only be validated through independent check points.

Methodology and case study field site

Precision maps for survey design: simulated UAV surveys

To demonstrate how precision can vary spatially and with survey characteristics, we first generated precision maps using rigorous photogrammetry software, for simulated UAV surveys with different georeferencing conditions and imaging geometries. The simulated surveys were constructed by initially defining camera models and positions over a virtual surface represented by a grid of 3-D tie points and GCPs. Image observations, including pseudo-random measurement noise to represent image residuals, were then generated for the tie points and GCPs, to complete the image network. Survey flight plans (based on those used in James and Robson (2014a)) were generated with two mutually inclined sets of parallel flight lines, which were augmented for some scenarios by twin gently banked turns in order to include convergent imagery, and hence add strength, to the image network (Figure 2, Table 1). The image networks were then processed by self-calibrating bundle adjustment using the close-range photogrammetry software ‘Vision Measurement System’ (VMS; http://www.geomsoft.com) which provides point precision as a standard output. The simulations were carried out for eight scenarios which covered the combinations of ‘weak’ or ‘strong’ control, for both GCPs or direct georeferencing using camera positions, and ‘weak’ (parallel-only) or ‘strong’ (augmented with oblique images taken with the same camera, from gently banked turns) image network geometries (Table 1). For the GCP-based simulations, the difference between ‘weak’ and ‘strong’ control scenarios was emphasised by also varying the image measurement precision of the tie points and GCPs (Table 1).

As well as measurement precision, the results enabled the actual surface error realised in each simulation to be assessed through direct comparison of the processed point positions with their known initial coordinates. Error in the overall georeferencing of surveys was determined by deriving the Helmert transform (the seven-parameter transformation for translation, rotation and scale) that best-fit the processed points to their initial positions. Applying the transform then allowed the residual surface shape error to be given by the remaining discrepancies with the initial coordinates (e.g. Carbonneau and Dietrich, 2016). Note that, in each instance, the errors calculated reflect the particular random offsets applied to the control and tie point measurements for that particular simulation. The errors realised thus represent a specific sampling from the distributions of likely error characterised by the precision values. Consequently, if a simulation was repeatedly processed with different random offsets each time, the distributions of error produced would reflect the precision estimates. Thus, when using SfM software that does not provide detailed precision information (but enables rapid and repeated bundle adjustment), precision estimates can be derived through such a Monte Carlo approach.

Implementing precision maps with SfM surveys

PhotoScan is currently the most commonly used SfM-based software for geomorphological surveys (Eltner*, et al.*, 2016) and supports automated analyses through Python scripts. In order to derive precision maps when using PhotoScan Pro (v. 1.2.3) we implemented a Monte Carlo-based approach (Figure 3, and see electronic supporting information for the Python script and instructions), with post-processing tools integrated into sfm_georef software (tinyurl.com/sfmgeoref; James and Robson, 2012). In summary, the method is founded on repeated bundle adjustments, in which pseudo-random error offsets are used to simulate observation measurement precision within the adjustment. Precision estimates for each optimised model parameter (e.g. each point coordinate or camera parameter value) are then derived by characterising the variance for each particular parameter in the outputs from a suitably large number of adjustments.

To start the analysis, images are processed as normal in PhotoScan: image alignment derives camera models, positions and orientations, and a sparse point cloud of 3-D tie points. During the alignment process, georeferencing can be achieved by either including ground control points or camera orientation data as control measurements, with (in version 1.2.3 of PhotoScan) all points or cameras accompanied by individual X, Y and Z components of measurement precision. The photogrammetric network is refined by identifying and removing outlier points, and ensuring that image observations of tie and control point measurements are appropriately weighted (i.e. appropriate values for the 'tie point accuracy' and 'marker accuracy' settings (James*, et al.*, 2017)). The resulting processed image network represents the geometry from which the dense image matching would be subsequently carried out to derive the DEM (a step that is not required within the Monte Carlo iterations, Figure 3).

The Monte Carlo analysis is underpinned by making a simulation copy of the image network which is internally error-free and, from which, each Monte Carlo iteration is then constructed by adding appropriate random error. The error-free network is derived by replacing all control measurements (e.g. surveyed GCP coordinates, or GPS-based camera positions and orientations if using direct georeferencing) with their network-estimated values, and by replacing all image observations with equivalents of zero-magnitude image residual by projecting the 3-D points into the cameras. For each iteration of the analysis, this error-free simulation copy is retrieved and offsets (error) are added to the observations and control measurements. The offsets appropriately represent the measurement precision by being derived from pseudo-random normal distributions with standard deviations given by the corresponding survey measurement precision or the RMS of the original image residuals. A bundle adjustment is carried out and the results exported to file before the next iteration is initiated.

The number of iterations to use can be determined by sequentially calculating the variance of the derived point coordinates, and carrying out sufficient iterations for variance estimates to stabilise. Finally, the results from all iterations are compiled to give distributions of determined values for all estimated parameters (e.g. coordinate values for each sparse point, camera model parameters and camera orientation parameters). To construct 3-D precision maps, point coordinate standard deviations (in X, Y and Z) are calculated for each point and interpolated onto a grid, resulting in three raster maps, representing the spatially variable precision in *X*, *Y* and *Z* directions. The influence of outliers (e.g. individual points that may be very poorly matched) is minimised by using a moving median filter for the interpolation, which determines the local median value over a defined radial distance. This is a reasonable first-order approach but certainly not the only possibility, and we leave exploration of alternatives to further work.

The Monte Carlo iterations not only enable precision values to be calculated but also the associated covariance. Thus, full point coordinate error ellipsoids can be derived for tie points, and correlation between camera parameters assessed (facilitating valuable checks for over-parameterisation of camera models). Furthermore, by considering the results of each iteration together as an entire surface model, the survey's overall georeferencing precision can be estimated – i.e. how precisely the surface is georeferenced in terms of its scale, translation and rotation. Interpretation of scale and translational precision is relatively straightforward, but rotational transformations are conventionally described by three angles that represent rotations applied sequentially around the *X*, *Y* and *Z* axes as the coordinate system is transformed (e.g. Förstner*, et al.*, 2013). However, their sequential application makes their values (Euler angles) difficult to interpret in field-geomorphological terms such as the resulting uncertainty in topographic slope. Thus, we calculate rotational precision directly in terms of the resulting slope uncertainty from the fixed *X* and *Y* axes of the geographic coordinate system (i.e. to give the precision of ground slope measurements in north-south and east-west directions), and a rotation around the *Z* axis. Finally, the precision estimates enable scale-independent estimates of overall survey quality to be calculated which, by reflecting conventional photogrammetric metrics, strongly facilitate inter-survey comparisons. We provide three such dimensionless relative precision ratios (for alternative suggestions see Eltner*, et al.* (2016) and Mosbrucker*, et al.* (2017)); firstly, mean point precision against the largest dimension in the survey (i.e. the distance between the furthest points), secondly, mean point precision against the mean viewing distance (e.g. James and Robson, 2012) and, lastly, mean point precision (as either the horizontal or vertical component) expressed in pixels.

Change detection with 3-D precision maps

With the spatially variable measurement precision given by maps of 3-D precision, confidence intervals for the detection of change between surveys can be determined. To maintain rigour when analysing complex topography, planimetric as well as vertical precision must be considered, and thus we compare dense 3-D point clouds directly, rather than using DEM products. Building on the current state-of-the-art, we base our approach on the full 3-D comparison of point cloud data implemented in the M3C2 algorithm (Lague*, et al.*, 2013). A detailed explanation of M3C2 is given by Lague*, et al.* (2013), but we summarise the method here in order to detail our precision map variant, M3C2-PM.

In M3C2, a local mean cloud-to-cloud distance is calculated for each selected point in the reference cloud. For speed, these 'core points' can be a subset of the original cloud. For each core point, i, the direction of the local surface normal, $\mathbf{N}$, is determined by fitting a plane to all its neighbours within a distance $D/2$ (Step 1, Figure 4). The position of the local surfaces in each point cloud is then calculated as the mean position of the cloud points that lie within a cylinder of diameter, d (Step 2, Figure 4), oriented along the normal direction, $\mathbf{N}$, giving two mean positions i_1 and i_2, separated by a distance $L_{M3C2}(i, d, D)$. For each cloud, the M3C2 algorithm uses the positional variability along $\mathbf{N}$ within these points (i.e. the local roughness in the normal direction) as a measure of uncertainty in their mean position, enabling a confidence interval (LoD) to be determined for the distance measurement. However, this assumes that the error in each point coordinate measurement is uncorrelated to that in nearby points and this will not be the case for photogrammetric point clouds, where error in adjacent point positions will be highly correlated due to the bundle adjustment process.

Thus, we adapt the M3C2 approach for use with photogrammetric point clouds by using M3C2 to determine local normal distances as usual, then incorporating 3-D precision estimates from associated precision maps (Step 3, Figure 4). Precision values (in *X*, *Y* and *Z*) are ascertained directly from the maps for the $i_1 - i_2$ point pairs, representing one-sigma axially-aligned error ellipsoids around each point (Figure 4). Based on established error analysis (Lane*, et al.*, 2003), and equivalent to Equation 1 in Lague*, et al.* (2013), $\text{LoD}_{95\%}$ can then be estimated by combining the precision components in the direction of the local surface normal, σ_{N1} and σ_{N2},

$$\text{LoD}_{95\%}(d) = \pm 1 \cdot 96\left(\sqrt{{\sigma_{\text{N1}}}^2 + {\sigma_{\text{N2}}}^2} + reg\right) \qquad 2),$$

where *reg* is the relative overall registration error between the surveys, assumed isotropic and spatially uniform (Lague*, et al.*, 2013). Note that Lague*, et al.* (2013) took a conservative approach by adding *reg* directly (as a potential systematic bias), which we retain here. Nevertheless, with the photogrammetric basis of σ_{N1} and σ_{N2} including georeferencing considerations, *reg* would be zero if both surveys were defined from the same datum. However, if there was uncertainty in the relative datum measurement between the different surveys, a non-zero value could be used. The output from M3C2-PM thus represents 3-D change between point clouds along local normal directions, along with an assessment of whether that change exceeds the local $\text{LoD}_{95\%}$ values, derived from the 3-D spatially variable photogrammetric and georeferencing precision.

Case study: Badlands site and data collection

To demonstrate precision maps and M3C2-PM for determining surface change in complex topography, we use a badlands case study from the River Cinca, Central Pyrenees, Spain (Smith and Vericat, 2015). Oblique images were captured of a ~4,700 m^2 catchment, during two surveys carried out from a piloted gyrocopter flown at ~50 m above ground level, in 2014 and 2015 (Table 2, Figure 5) and processed using GCPs for control (e.g. Figure 5b inset).

In 2014, GCP positions were measured by GNSS (a Leica Viva GS15 in RTK mode) to give absolute positions and associated precisions (ranging between ±7 mm to ±29 mm in the horizontal, and ±14 m to ±41 m in the vertical) which were converted into ED50 UTM (Zone 31 N) coordinates. In 2015, GCP positions were measured with a Leica TPS1200 total station, giving coordinate precision estimates relative to the instrument position. Thus, when converting these into UTM, the uncertainty in the absolute position of the instrument had to be accounted for: the total station position was derived by resection to a primary control network comprising four permanent targets, giving an RMSE of 9 mm (although note that such few targets make reliable RMSE estimation difficult due to comprising only one redundant point). With the primary control network having a mean absolute 3-D quality of 6 mm (see Smith and Vericat (2015) for details), we use an overall value of 11 mm for the absolute precision of the total station position in UTM coordinates.

In 2014, benchmark TLS data were acquired for comparison (Smith and Vericat, 2015) using a Leica C10 with a maximum measurement range of 300 m and manufacturer-stated precisions of 6 mm for position, 4 mm for distance, and 60 μrad for angle. To minimise gaps caused by occlusion, data from twelve different stations were combined using target-based registration (with 2 mm mean error), based on a floating network of tripod-mounted Leica targets. The target coordinates were measured with the total station which, in turn was registered to the primary control network as in 2015. Thus, UTM precision estimates for the TLS survey were not straightforward, and we use 11 mm for uncertainty in the datum (as for the total station) and a conservative 10 mm for within-survey precision, to cover all instrument measurement and relative scan registration components.

Data processing and analysis

Images were processed in PhotoScan (v.1.2.3). Image observations of the GCPs were collected using a semi-automated oriented patch cross-correlation approach (James*, et al.*, 2017) and network quality checks during initial processing (James*, et al.*, 2017) suggested that three GCPs needed to be rejected from the 2014 network as outliers. For both surveys, initial tests for camera model over-parameterisation were carried out based on GCP analysis (James*, et al.*, 2017), and suggested that the optimal camera model comprised focal length, principal point and three radial distortion components (denoted as Model A). To ensure appropriately balanced optimisation within the surveys, the 'marker accuracy' and 'tie point accuracy' processing settings were given the values of the RMS image residual magnitudes on GCPs and tie points respectively (James*, et al.*, 2017). Other PhotoScan processing settings used were: photos aligned with accuracy 'high', pair preselection 'generic', a tie point limit set to 5000 (to help give a dense distribution of tie points for precision analysis), and the coordinate system set to ED50 UTM (Zone 31 N). The Monte Carlo processing comprised 4,000 iterations for each survey (taking ~3·5 hrs per survey on a desktop PC), and the resulting point precision estimates were interpolated over a 1100 × 700 m, 1-m-resolution grid to cover the catchment of interest. Following the precision analysis, dense cloud generation was carried out at 'high' quality, with 'aggressive' depth filtering to minimise surface noise.

The 2014 SfM survey data were used initially to validate the Monte Carlo approach by comparing the resulting precision estimates with values generated directly by reprocessing the PhotoScan survey in VMS. The survey was also processed using a more complex camera model (Model B, that additionally included two tangential distortion parameters) to verify the choice of camera model and to check for over-parameterisation through assessing the camera parameter correlations and precision information delivered by the Monte Carlo analysis.

The SfM survey was then compared to the benchmark TLS survey over the extent of the TLS data, and with areas of denser vegetation cover removed. As an initial assessment of the M3C2-PM approach, four comparisons were carried out: a straightforward DoD, a DoD using a survey-wide $LoD_{95\%}$ and then 3-D cloud-to-cloud comparisons using M3C2 and M3C2-PM. For the DoD comparisons, 0·1-m-resolution DEMs were derived from the dense point clouds using average elevation values in CloudCompare v.2.7.0 (cloudcompare.org). The survey-wide $LoD_{95\%}$ was introduced by conventionally estimating the overall vertical measurement precision of the surveys as 14.9 mm for TLS (the datum uncertainty and within-survey precision added in quadrature) and 36.8 mm for the SfM (based on the *Z*-RMSE on control points, Table 2), giving $LoD_{95\%}$ = 78 mm (Equation 1). To consider 3-D differences, the native M3C2 analysis was run on the underlying point clouds in CloudCompare. Throughout this work, *D* and *d* (Figure 4) values of 0.3 m were used to provide areas sufficiently large for good calculation of surface normal but not too large to be adversely affected at slope-scale (the roughness scales of the badland topography can be considered from Figure 5). A *reg* value of 80 mm was used, based on combining the 3-D RMSE on the SfM control points (79 mm) and the TLS instrument position precision (11 mm), in quadrature. When using M3C2-PM, the photogrammetric and georeferencing precision of the SfM survey was integral within the precision maps, so *reg* only represented the uncertainty in the TLS instrument position (11 mm). The TLS data did not have associated precision maps, so a constant value of 10 mm was used to represent their precision within the survey.

The potential for future SfM surveys to be directly georeferenced was investigated by removing the GCPs from the survey processing and using the estimated camera positions as control measurements. Survey precision was then evaluated by carrying out bundle adjustments in VMS with different precision values assigned to the camera position values. Equivalent analyses were also carried out in PhotoScan using the Monte Carlo approach, by applying offsets from pseudo-random distributions (of appropriate standard deviations) to the camera position control data for each Monte Carlo iteration. The results were compared with those from GCP-based georeferencing, with the influence of measurement precision also assessed by varying the precision assigned to the GCPs.

Finally, sediment budgets between 2014 and 2015 were derived from the SfM surveys using the same four analyses as the SfM-TLS comparison. A single survey-wide $LoD_{95\%}$ of 80 mm was determined by adding in quadrature the vertical RMS discrepancies on GCPs (on either check or control points, whichever was the greater), and the 11 mm uncertainty in total station instrument position for the 2015 survey. For M3C2 processing, using the 3-D RMS discrepancies on GCPs (79 mm for 2014, and 27 mm for 2015, including the total station instrument position precision) as estimates of georeferencing precision resulted in *reg* = 83 mm. Finally, for our M3C2-PM approach, with point precision estimates explicitly including survey georeferencing, *reg* comprised only the total station instrument position precision for the 2015 survey (11 mm).

Results

Simulated surveys: precision maps and spatial variation

For a simulated UAV survey with weak image network geometry, but strongly georeferenced using GCPs measured to a precision representative of dGPS measurement (Table 1), 3-D point coordinate precisions showed correlations with changes in image overlap (Figure 6a), indicating that precision was being limited by photogrammetric considerations (i.e. the image network geometry, Figure 1b). Error analysis demonstrated the network geometry weakness by identifying systematic doming as surface shape error, which was present despite the use of ground control in the bundle adjustment (Figure 6a). Strengthening the network geometry by including oblique imagery mitigated the doming (James and Robson, 2014a) and generally improved precision through increasing image overlap (Figure 6b). In this case, the well-distributed and precise GCPs provided a strong overall georeferencing of the survey; error in horizontal position was <3 mm and ground slope error (reflecting systematically varying height error) was <0·005° (Figure 6b), representing height errors of <6 mm at the GCPs furthest from the survey centre.

If GCPs were only surveyed to relatively poor precision (e.g. 50 mm in *X* and *Y*, and 100 mm in *Z*, Figure 6c) then the weak control would limit overall survey precision (i.e. just as illustrated in the schematic Figure 1c), even if high-quality tie points and strong network geometry mean that the overall surface shape showed little error (Figure 6d). In this case, the strong photogrammetry would provide high precision internal measurements, such as relative line lengths, but the surface was weakly georeferenced within the external coordinate system (e.g. with systematic error in horizontal position of up to 14 mm and slope error of 0·04° shown in Figure 6d, which could be critical when estimating changes of sediment distribution in areas of steep terrain, or flow directions in flat terrain). The symmetric radial degradation of precision away from the centroid of GCP control (Figure 6c, d) reflects this uncertainty in overall georeferencing, and is a combination of scale, translational and rotational uncertainty about the centroid of the control measurements (Figure 1c), which is where the datum is defined during the bundle adjustment.

Similar relationships were demonstrated for surveys directly georeferenced using knowledge of camera positions – i.e. without the use of GCPs as control points. If on-board dGPS could provide relatively precise camera position data (e.g. 20 mm in the horizontal and 40 mm in the vertical, and carefully synchronised with image acquisition), then survey precision and overall georeferencing error achieved levels equivalent to those given when using the GCPs (Figure 7a, b), although note that this is strongly dependent on the number and spatial distribution of images. However, currently, UAV camera positions are not generally known to such precision (e.g. the GPS on a consumer UAV may provide position at a precision closer to ~2 m in the horizontal and ~4 m in the vertical (Chiang*, et al.*, 2012), in which case 3-D point precision is strongly limited (Figure 7c, d), with weak network geometries developing systematic error in surface shape (Figure 7c). Overall georeferencing errors were represented by horizontal translations and slopes of up to ~0·5 m and 0·5° respectively.

Thus, precision maps enable valuable insight into predicted survey performance, and therefore represent a useful survey planning tool that highlights the relative influence of photogrammetric (e.g. tie points, imaging geometry) and georeferencing (e.g. control points) aspects in overall survey quality.

Badlands surveys: Precision maps and TLS comparison

For the 2014 SfM badlands survey, the Monte Carlo results showed that 4,000 iterations were sufficient to ensure that uncertainty in the point coordinate precision estimates was of order 1 mm (Figure 8a). The coordinate precision values for all tie points were up to ~0·5 m, and demonstrated strong correspondence with the precision estimates made by rigorous bundle adjustment in VMS (Figure 8b), validating the SfM-Monte Carlo approach. The large values were generally located at the survey extents (i.e. similar to the simulations in Figure 6), and far from the catchment of interest and region of GCP deployment (Figure 5d). Over the region immediately surrounding the catchment (i.e. Figure 5e), mean point precisions were ~23 and 26 mm in the horizontal and vertical respectively, with overall survey georeferencing determined to precisions of <6 mm in translation and <0·02° in topographic slope (Table 3) – note that such slope uncertainty represents a vertical precision of 16 mm at a distance of 50 m from the centroid of control.

Precision estimates for the camera parameters showed that all parameter values were well resolved (i.e. their magnitudes were much greater than their precisions, Table 3). Assessing correlations between parameters to give insight into any self-calibration problems indicated that, with one exception, parameter correlations were in line with expectations of a good network, with generally small magnitudes, excluding between the radial distortion terms (Table 4, Camera model A). The block of high-magnitude correlations between radial terms is usual, and results directly from the polynomial representation of the radial distortion model (Clarke and Fryer, 1998; Tang and Fritsch, 2013). The exception was the abnormally high correlation between the principal point offset in *y* and the principal distance. This suggests a slight network weakness that is usually associated with the absence of large camera rotations (i.e. a lack of images taken from similar positions, with 'portrait' as well as 'landscape' orientations, which is often omitted in UAV surveys); a detailed analysis is out of scope of this paper but see Luhmann*, et al.* (2006) for further information on camera calibration. When the more complex camera model was used (Table 4, Model B), the correlation analysis clearly demonstrated that the increased number of parameters was not appropriate; when tangential distortion terms were included, they showed high correlations with principal point and principal distance terms and no improvements to tie point RMSE or fit to check points were observed. Thus, Model B was deemed over-parameterised and Model A was retained, supporting the initial GCP-based assessment.

The relative precision estimates for the full survey indicated that, in comparison with previously published SfM work, it was towards the high-quality end, with a ratio of mean precision against mean observation distance of 1:4,100 (Table 3). The geometric combination of oblique views from the gyrocopter also resulted in vertical precision being slightly better than the horizontal component. Over the region of interest, the interpolated precision maps showed point precision magnitudes <0·15 m (Figure 9) and strong local variability that dominated any broader structural survey variations. The areas of poor precision correspond to areas of vegetation (compare Figure 9a and b), and resulted from the fewer observations made for points in these areas (Figure 9c and f).

With the 2014 SfM and TLS surveys being effectively simultaneously acquired, differences between them should fall appropriately within the estimated confidence bounds. Straightforward DoD comparison shows systematic differences which highlight east to north-east facing steep gully walls, and are indicative of horizontal error in the relative georeferencing of the surveys (Figure 10a). Using a survey-wide $LoD_{95\%}$ retained these systematic significant differences, due to horizontal error remaining neglected (Figure 10b).

With 3-D analysis using native M3C2 algorithm, nearly all the differences between the surfaces fall within the large uncertainty dominated by the rather conservative *reg* term (Figure 10c). Using the precision maps adaptation, M3C2-PM, more regions of significant difference were highlighted (Figure 9d), but nevertheless, the approach substantially reduced the effects of horizontal error (c.f. Figure 10b). Many of the areas where differences exceeded the local 3-D $LoD_{95\%}$ are located at the bottoms of gullies and their tributaries, and have been previously identified as the least accurate in the SfM survey (Smith and Vericat, 2015), and could potentially have been affected by smoothing during the dense image matching stage.

Predicted survey performance under direct georeferencing

Reprocessing the 2014 SfM survey to simulate direct georeferencing showed that, over the area of interest, similar point precisions could be achieved when the prescribed camera position precision was similar to that of the GCP field measurements (Figure 11). However, knowing camera positions more precisely geve little gain, because photogrammetric considerations, such as image measurement precision of tie points, were the limiting factor (i.e. just as in Figure 1b). To understand the best possible precision that could be achieved with the images, the survey was also processed by removing all control data prior to a bundle adjustment, to give an 'inner constraints' adjustment which provides precision values within a local coordinate system defined by the initial coordinate values of the tie points alone, (i.e. Figure 1a). This resulted in a mean vertical point precision of 23 mm, with 10% and 90% bounds of 8 and 50 mm (the grey band, Figure 11). Thus, when including control measurements in order to georeference the survey, deviations from this optimum can be considered as dilution of the achievable precision due to the introduction of control that is weaker than the underlying tie point photogrammetry (i.e. as in Figure 1c).

Weakening the camera position precision led to degraded 3-D point precision, reflecting a weak overall georeferencing (Figure 11, in the same manner as illustrated in Figures 1c and 7c, d). The same effect was shown for GCP-based georeferencing (Figure 11) but, with more camera positions (and more broadly distributed) than GCPs, then overall point precision was less sensitive to control measurement precision under direct georeferencing. For direct georeferencing, control measurement precision became an overall limiting factor at weaker control precision values than for GCP georeferencing. Furthermore, once point precision was limited by control measurement, point precision was approximately three times better from direct georeferencing than from using GCPs (Figure 11).

Change detection with 3-D precision maps

Changes between the 2014 and 2015 surveys (Figure 12, Table 5) were greatest when calculated by straightforward DoD (Figure 12a), which showed a general sub-decimetre lowering of the surface between 2014 and 2015, but with some systematic height increases associated with steeper slopes, indicative of error in the relative horizontal registration of the two surveys. Using a single survey-wide $LoD_{95\%}$ accommodated much of the overall lowering within the estimate of measurement precision, but notable areas of systematic height increase remained (Figure 12b).

In contrast, the native M3C2 algorithm identified only a very few areas where change exceeded the local 3-D $LoD_{95\%}$ value (Figure 12c), giving results that are out of step with field observations of active sediment transport through the main thalwegs of the study area. Finally, the M3C2-PM approach (Figure 12d) delivered the most plausible distribution of topographic change of the methods tested, with minimal areas of apparent upward change resulting from unaccounted-for horizontal error on steep slopes, and volume losses dominantly restricted to gully bottoms and tributaries.

Discussion

Our results have indicated that considering 3-D precision improves change detection in areas of complex topography. The detected pattern of sediment loss within the badland catchment is very similar to that observed in TLS data over the previous year (i.e. between 2013 and 2014, see Smith and Vericat, 2015); however, the calculated average topographic change of -18·2 mm a^{-1} (Table 5) is far greater than that calculated for 2013 to 2014 (-1·44 mm a^{-1}). With sediment erosion and transport in badlands known to be concentrated in individual high-magnitude rainfall events (e.g. Cantón*, et al.*, 2001), analysis of the rainfall record confirms that the 2014 to 2015 monitoring period exhibited six storms of a greater intensity (~40 mm hr^{-1} over a 15 minute interval) than any in the previous year. Moreover, when converted to sediment yield (272 t $ha^{-1}a^{-1}$ over a 0·471 ha area) it is in line with erosion rates measured elsewhere in Mediterranean badlands (Nadal-Romero*, et al.*, 2011). Thus, 3-D precision maps facilitate robust geomorphological analysis and could be used to design survey campaigns that achieve specific $LoD_{95\%}$ values across an area. They also provide insight into the factors behind precision variability between and within surveys, and can indicate whether photogrammetric or georeferencing aspects are overall limiting factors.

Interpreting precision maps

Point precision is affected by range of factors that we have considered as either 'photogrammetric' (i.e. internal to the photogrammetric network, such as imaging geometry and the quality of the tie point identification within the images, Figure 1a) or related to the georeferencing (e.g. the external control measurements which limit precision in Figure 1c).

Precision maps showing broad, systematic variations (e.g. Figure 6c, d) indicate weakness in overall survey georeferencing (i.e. as Figure 1c), symptomatic of weak control. This can either be due to the poor precision of control measurements, or because control is poorly distributed (e.g. too few, or insufficiently spaced, control measurements). For an imaging geometry appropriate to aerial surveys, the degradation in precision away from the centroid of control measurements (Figure 6c, d) is likely to dominantly reflect uncertainty in the rotational component of overall georeferencing, and indicate the probability of slope error in a DEM (e.g. Carbonneau and Dietrich, 2016). More control, or control more widely distributed or measured to better precision, will improve overall rotational georeferencing precision, and may result in uncertainty in scale and translational components dominating point precision estimates. Forecasting improvements in rotation and scale will not be straightforward and will depend on the quality, locations and number of additional measurements. In contrast, and based on straightforward error statistics (e.g. Borradaile, 2003), translational precision should approximate to $n^{-1/2}$ of the control measurement precision, where *n* is the number of control measurements.

If precision maps indicate strong localised variations, then photogrammetric factors are being expressed, e.g. differences in image measurement quality for individual tie points, and image network geometry aspects such as image overlap and convergence (e.g. Figure 6a, and badlands survey, Figure 9b). Weak precision will result from small numbers of observations for a point, from similar positions (i.e. narrow angles of ray convergence); image matching can be hindered by too large separation of images. Thus, such variations can highlight areas of poor image coverage (e.g. resulting from partial occlusions in complex terrain), or regions of more challenging image matching, such as due to vegetation (Figure 9a, b). Identifying these areas through carrying out a preliminary survey would enable enhanced survey designs to ensure precision requirements can be met across the full area.

For the badlands survey, overall point precision over the full extent of the sparse point cloud was limited by the control, due to GCP deployment being spatially restricted to the central region of interest (Figure 5). However, within the area of interest, the GCPs provided strong constraints, and variations in point precision reflected local differences in the number (and probably quality) of image observations per point. Weak matching in zones of vegetation resulted in the areas of worst precision, and error ellipses indicated precision differences due to the complex topography being viewed from different directions. With the control measurements not being the limiting factor over the region of interest, fewer GCPs could have been used without substantial effect on overall point precisions. Using the Monte Carlo analysis of James*, et al.* (2017), specifically aimed at analysing GCP performance and identifying minimum numbers, indicated that survey quality would be maintained with only 8 GCPs. This figure is in line with the current work where, for a mean GCP measurement precision of 26 mm, 8 GCPs would provide a translational precision of <10 mm, so (assuming the GCPs were suitably distributed) overall survey precision would remain limited by photogrammetric considerations (Figure 11).

Direct georeferencing versus GCPs

Photogrammetric best practice recommends that control measurements are distributed across and surrounding the volume encompassing the survey area (Luhmann*, et al.*, 2006). When using GCPs, tie and control points are ground-based and the influence of control on the interpretation of precision maps is relatively straightforward to consider (as described above) because the control is in close proximity to the surveyed points. Note that the effects of GCP precision and distribution on survey quality have been well studied within conventional aerial photogrammetry (Krauss, 1993). For direct georeferencing of typical aerial surveys, the use of camera positions as control displaces the control measurements above the survey volume. In this case, positional error can be effectively magnified within the survey region due to the effects of angular uncertainty in overall georeferencing being enhanced along the observation distance. This issue reduces as the span over which images are acquired increases with respect to the observation distance, i.e. as the distance along or across imaging flight paths increases, with respect to the flying height. Thus, for direct georeferencing, with all other things equal, wider flight patterns, capturing convergent imaging of a central, localised region (as in the badlands case study, Figure 5d) would be recommended (Figure 13).

To improve precision when direct georeferencing, capturing more images represents an efficient way to acquire more control measurements. In the simulations and case study here, there were ~4–8 times more images than GCPs. Thus, in line with the $n^{-½}$ argument and for equally precise control measurements, survey precision under direct georeferencing could be 2–3 times better than from GCP-control (e.g. Figure 11). Alternatively, camera positions could be measured to approximately only half to a third of the quality of the GCPs, to achieve a similar overall point precision. This could be diluted further if more images were acquired, albeit with diminishing returns; it may be feasible to improve precision by an order of magnitude through capturing 100 rather than 10 images, but the ~1000 images required for another order of magnitude improvement could have disadvantages for practical image acquisition and rapid data processing. Nevertheless, in most cases, camera position cannot be measured as precisely as a ground point due to the specific GPS (or other) measurement technologies involved, thus, acquiring more images is likely to be a useful strategy for direct georeferencing deployments. Improving the georeferencing will enable the overall survey precision to be enhanced up to the point that precision becomes limited by the photogrammetric considerations (i.e. imaging geometry, quality of the tie points etc.) rather than the control measurements (such as for the GCP-case illustrated in Figure 1b).

In this work, the use of only camera positions in direct georeferencing has been explored, but measurements of camera orientation can also be included in the process (e.g. Cramer*, et al.*, 2000). However, in the GCP-georeferenced badlands survey, the processed image network provided camera rotations with precision estimates of order 10^{-2} degrees (Table 3), which is approximately two orders of magnitude better than delivered by current UAV-suitable orientation sensors (Gabrlik, 2015; Pfeifer*, et al.*, 2012). Thus, first indications are that practical measurements of camera orientation may not currently be able to add to the quality of the results. Nevertheless, due to the interdependencies between camera position and orientation within photogrammetric processing, the precision of derived values is no guarantee of the effectiveness of using measurements as control, and including orientation data could be an area for further research. As an example of such complexity, it is interesting to note that using camera positions as control appeared more effective at mitigating the doming error than GCPs, even when the GCPs were measured with twice as good precision (compare the 'Shape' plots in Figure 6a and 7a).

For the badlands survey, the camera locations widely bracketed the region of interest (Figure 5), reducing the influence of rotational components of overall georeferencing uncertainty on point precision. Thus, for direct georeferencing using poor precision camera positions, point precision may be expected to reflect translational uncertainty, with magnitudes approximating to $n^{-½}$ × camera position precision. This is shown for camera position precision values exceeding ~200 mm (Figure 11), where (for 104 images) mean point precisions approach ~0·1 × camera position precision. Thus, directly georeferencing the survey using multi-metre precision camera position measurements (typical of a consumer UAV) would have resulted in multi-decimetre point precision, but using camera position observations known to ~0·1 m would be expected to achieve similar overall precision as from the GCP array.

In contrast, for GCP-based georeferencing under sufficiently weak control that it limited overall survey precision, then rotational georeferencing components formed an import contribution to dilute point precision, due to the GCP distribution being more spatially restricted than the camera positions. Consequently, mean point precision values did not approach the $n^{-½}$ × control precision limit (the uppermost dashed line for 19 control points in Figure 11).

Camera models, parameter correlations and quality control

The additional camera parameter precision and correlation information provided either by the Monte Carlo approach (or now directly available within the most recent version of PhotoScan v.1.2.6) promotes rigorous quality assessment of self-calibrating image networks through enabling good practice checks. For topographic surveys, these checks should be carried out before the dense matching (MVS) in an SfM-based workflow:

1) All camera parameters included in the camera model should improve the results (i.e. their use in the camera model should reduce RMS image residuals and check point discrepancies).

2) All camera parameter magnitudes should exceed the precision to which they are determined. Parameters that fail this test, or have a magnitude of the same order as their precision, should have their value fixed at zero (i.e. the parameter is inactive and removed from optimisation) and the self-calibration analysis run again (e.g. Granshaw, 1980).

3) Camera parameters should be checked for high magnitude correlations between them (i.e. Table 4). Strong correlations between camera parameters are likely to indicate weakness in the image network that result in the relative effects of the different parameters being inseparable. Where such strong correlations exist, the importance of the parameter pair can be tested by observing whether results deteriorate if one of the parameters is removed from the optimisation. If they do, the parameter can be reinstated, but if not, then it can be fixed at zero to avoid over-parameterisation of the camera model. Note that radial distortion parameters are expected to be strongly correlated (Clarke and Fryer, 1998; Tang and Fritsch, 2013); nevertheless, two are likely to be useful for most consumer cameras (for a detailed analysis, see Wackrow*, et al.* (2007)).

4) Alongside checks for images with systematic or large magnitude tie point image residuals (James*, et al.*, 2017), camera orientation (precision in position and direction) can be used to test for poorly constrained images. Photographs that show anomalously weak orientations can be considered for removal from the network, because they will not be adding to the strength of the network, and may be contributing to surface error.

Integrating precision into DEM uncertainty processing

Precision maps represent a valuable tool for propagating spatially variable precision in modern SfM surveys forward into established uncertainty-based DEM workflows. Although we use a fully 3-D method for change detection, our interpolated precision maps are also well placed for direct integration with conventional 2.5-D DEM processing. Such an approach may be suitable in areas where topography is sufficiently flat that horizontal precision components may be neglected. However, with precision estimates underpinned by Gaussian statistics, they could be optimistic in some difficult field scenarios. In these cases, precision information can be considered within existing approaches based on fuzzy inference, along with other information such as orthoimage colour or texture to enhance the spatial context (e.g. Wheaton*, et al.*, 2010). Thus, precision maps should form a first step from which other uncertainties inherent within DEM processing (e.g. Wechsler, 2007) can also be considered.

Conclusions

SfM-based surveys are increasingly facilitating routine acquisition of high resolution topographic models, and are transforming data collection practices across environmental and geomorphological research. However, with this, and with photogrammetric processing usually concealed within 'black box' software, the requirement for greater understanding of the associated uncertainties becomes more pressing. Our robust 3-D detection of topographic change is built on precision maps that also facilitate understanding of the fundamental survey characteristics that affect measurements. Such understanding is vital for optimising future work through improving survey planning and for more informed decision-making for GCP deployment or the use of direct georeferencing. By providing access to the metrics that are routinely used for network quality control in metric photogrammetry (such as camera parameter precisions, correlations and point error ellipsoids), our Monte Carlo approach offers a substantial advance for rigorous topographic measurement using SfM. Although the Monte Carlo analysis requires several thousand bundle adjustments, the subsequent dense matching is likely to remain the slowest stage within a complete workflow. Hopefully, future SfM software will both integrate and expose rigorous precision analysis (as PhotoScan v.1.2.6 now does for camera parameters), and precision maps will become a standard component of topographic models and subsequent processing. By applying our method, we show that:

1) In areas of complex topography and steep slopes, estimates of sediment budget from photo-based surveys can be substantially improved by considering the 3-D and spatially variable survey precision, when deriving confidence intervals for change detection.
2) Such analyses are enabled by 3-D precision maps which integrate the photogrammetric and georeferencing contributions to photo-based survey precision. The interpretation of precision maps gives insight into the precision-limiting factors, thus, a simulation or analysis of a preliminary survey is recommended to optimise survey design.
3) Precision estimates that vary smoothly across a survey (e.g. Figure 6c, d and 7c, d) indicate that control measurements are the dominant factor (Figure 1c) and that survey precision could be improved through enhanced survey control (e.g. more GCPs or better measured camera positions, Figure 13b, c). When rotational components of georeferencing are not contributing substantially to point precisions, then overall point precision may be estimated as $n^{-½}$ × control precision (Figure 11).
4) If precision maps show details that reflect characteristics such as changes in image overlap (e.g. Figure 6c, d and 7c, d) or surface features such as vegetation (e.g. Figure 5) then survey precision is being dominated by

photogrammetric considerations. In this case, improving control is unlikely to be worthwhile, but gains are likely to be made by improving image measurements (e.g. removing tie points with few observations or with large image residuals) or by strengthening the image network geometry (Figure 13a).

As the use of SfM-based techniques in geomorphology matures, there will be increased demand for the characteristic ease of data capture and flexibility of SfM software to be combined with the rigorous uncertainty estimates exemplified by traditional photogrammetry. Precision maps and 3-D confidence-bounded surface change detection through M3C2-PM facilitate the use of such photogrammetric uncertainty estimates in a geomorphology context, and our Monte Carlo approach provides this capability for current SfM workflows.

Acknowledgements

We thank Damià Vericat for providing the TLS data and for fieldwork assistance. Dimitri Lague and Trevor Page are gratefully acknowledged for discussions on M3C2 and uncertainty respectively. Badland surveys are supported by grants from the British Society for Geomorphology, embedded within the framework of MorphSed, a research project funded by the Spanish Ministry of Economy and Competiveness and the European Regional Development Fund (CGL2012-36394). We thank the Associate Editor, A. Eltner and an anonymous reviewer for highly constructive comments that have helped clarify the manuscript throughout.

Figures

Figure 1. Survey precision and georeferencing; all panels are purely illustrative 2-D sketches only. (a) Processing photo-based surveys enables the positions of tie points (black circles) to be determined on the topographic surface (dark grey line) through observing the points in different images. Uncertainty in the tie point positions can be represented by error ellipsoids (enlarged for visibility) which, through their size and orientation, reflect the different contributions to photogrammetric uncertainty, such as the network geometry and image measurement precision. Overall, the tie point uncertainties result in uncertainty within the shape of the derived surface, as illustrated by the light grey bands surrounding the darker grey line. (b) When the survey is georeferenced (e.g. through the inclusion of GCPs as control measurements, shown by black ellipses) precision is given in the geographic coordinate system. If control precision is better than the precision from the photogrammetry (i.e. better than in (a)), then precision estimates retain the variations due to the underlying photogrammetric considerations. (c) However, if control is weak (e.g. GCPs are measured to poor precision) then precision in the geographic coordinate system can become limited by the control measurements. The surface will retain the shape derived by the tie point photogrammetry (i.e. in (a)), but its transform into geographic coordinates will effectively be subject to large uncertainties in scale, translation and rotation.

Figure 2. Schematics of the flight path and image footprints for the simulated UAV surveys. (a) Flight paths are illustrated using dark blue cones to show the locations of image acquisitions along twin sets of parallel flight lines. Red cones show the positions of additional acquisitions for simulations that involved two gently banked

turns to include oblique (20° to the vertical) imagery (see Table 1 and James and Robson (2014a) for details). (b) Corresponding image footprints, with black triangles indicating GCP locations.

Figure 3. Workflow for confidence-bounded 3-D change detection with SfM surveys and precision maps. See Figure 4 for further details on the M3C2-PM approach.

Figure 4. Change detection in photogrammetric point clouds with M3C2-PM. Steps 1 and 2 represent use of the M3C2 algorithm (Lague*, et al.*, 2013) to identify local normal directions between point clouds and determine the local mean separation distance in this direction, L_{M3C2}. In Step 3, the adapted M3C2-PM approach uses photogrammetric precision estimates to derive a confidence interval (or LoD) for this distance measurement. Each mean point, i_1 and i_2, is associated with precision estimates in the X, Y and Z directions, representing an error ellipsoid. The confidence interval for distance measured in the normal direction, **N**, is then determined using the components of precision in that direction, σ_{N1} and σ_{N2} (Equation 2). Redrawn in part from Lague*, et al.* (2013).

Figure 5. The 2014 badlands survey. (a, b) Examples of the aerial images captured with the inset (80 × 50 pixels) showing a GCP target. From the ground, an example eroding headcut (c) shows the high local relief and steep slopes, with the influence of differing compactness within the structured Eocene marl sequence being apparent on the surface form (for scale, the square red targets are 200 × 200 mm). (d) A perspective view of the rendered topographic model and camera positions, showing the wider distribution of tie points. (e) The associated DEM visualised by hill-shade

and overlaid with GCP positions (note that 4 GCPs were outside this extent); triangles for control points, and circles for check points.

Figure 6. Precision and vertical error maps for simulated UAV surveys georeferenced using GCPs. Four survey scenarios, represented by the rows, are characterised by strong (a, b) or weak (c, d) ground control (Table 1, with ‘strong’ control representative of using dGPS-measured targets as GCPs), and the inclusion (b, d) or not (a, c) of banked turns in the flight plan (Figure 2). GCP locations are indicated by the triangle symbols and the inset value in the top right of each precision plot gives the mean tie point precision (in mm) within the region encompassed by the dashed line in (a). Error contributions were determined by deriving, then applying the Helmert transform that best-fitted the processed points to their initial, simulated positions. The overall georeferencing error component is then the change in point coordinates given by the Helmert transform, and the surface shape error is given by the remaining discrepancies. Note that only vertical components are shown.

Figure 7. Precision and vertical error maps for simulated UAV surveys directly georeferenced using camera position coordinates. The four survey scenarios, represented by the rows, are characterised by strong (a, b) or weak (c, d) georeferencing (as determined by the simulated precision of camera position measurements, with ‘weak’ representative of data from a consumer-grade UAV, Table 1), and the inclusion (b, d) or not (a, c) of banked turns in the flight plan (Figure 2). Note the one to two orders of magnitude differences between the colour scales of the weak and strong scenarios. The value inset in the top right of each precision plot gives the mean tie point precision (in mm) within the region

encompassed by the dashed line in (a), for comparison with Figure 6. Surface error was calculated just as for Figure 6.

Figure 8. (a) Variability in SfM-Monte Carlo tie point precision estimates as a function of the number of iterations in the Monte Carlo analysis. Each plotted line shows the difference in estimated precision for a tie point, from the final estimate for that point made after 4,000 iterations. (b) Estimates of point coordinate precision components in *X*, *Y* and *Z*, as determined from the SfM-Monte Carlo approach (with 4,000 iterations) are validated by their correspondence with those provided directly by least squares bundle adjustment in VMS (each plotted symbol represents the precision estimate for one tie point). Grey lines represent 1:1 ratios for visual reference.

Figure 9. Precision maps for the 2014 badlands survey. The survey orthomosaic (a) gives spatial reference for the summary map of precision magnitude (b), as interpolated from tie points (the inset text gives the mean value). Excerpts of typical image texture (300 × 300 pix) show that bare topography can provide good precision (blue) and that areas of weakest precision (yellow) mostly reflect vegetation cover. (c) The tie point locations used for map construction, coloured by the number of images in which each point has been observed (note the $\log_{10}$ colour scale). The underlying point precision data can be provided as *X*, *Y* and *Z* components, shown by histograms (d, with inset mean values), precision maps (e), or by a 3-D error ellipsoid for each point. Projecting error ellipsoids on a cross section (f, for points within 1 m of the section A-A' in (a-c)), underscores that the weakest points are derived from few, and generally oblique, observations.

Figure 10. Vertical differences between the 2014 TLS and SfM-based surveys determined using different methods for comparison. All plots are cropped to remove areas of vegetation and are given at a horizontal resolution of 0·1 m, overlying a hill shade image. In areas where change is determined to be significant, vertical change is overlain in colour. (a) Straightforward DEM of difference. (b) As (a), but transparent where DoD values are smaller than an $LoD_{95\%}$ of 78 mm. (c and d) As (a), but showing only areas where the original point clouds were detected to be significantly different by M3C2 (c) or M3C2-PM (d).

Figure 11. Tie point precision statistics for the region of interest of the badlands survey, for different assumed values of mean control measurement precision. Mean point precision values (symbols) are bracketed by 10^{th} and 90^{th} percentile bars. For direct georeferencing (using camera positions as control measurement), the overlying symbols illustrate that the PhotoScan results are almost indistinguishable from those from VMS. All results for GCP-georeferencing were processed with PhotoScan only, using the selected GCPs indicated in the underlying distribution maps as control. The results associated with dashed bars are for the GCP precision values of the field data. The dashed horizontal line (mean) and grey band (10^{th} and 90^{th} percentiles) give the point precision derived in the absence of any control measurements (i.e. Figure 1a). This 'inner constraints' bundle adjustment indicates the best point coordinate precision that could be achieved with this survey's tie point image measurements and image network geometry. The inclined long-dashed lines represent point position precisions of $n^{-½}$ × control measurement precision, for n = 19 (upper line, reflecting 19 GCPs) and n = 104 (lower line, reflecting the number of camera positions).

Figure 12. Vertical change between the 2014 and 2015 SfM-based surveys determined using different methods for comparison. All plots are cropped to remove areas of vegetation and are given at a horizontal resolution of 0·1 m, overlying a hill shade image. In areas where change is determined to be significant, vertical change is overlain in colour. (a) Straightforward DEM of difference. (b) As (a), but transparent where DoD values are smaller than an $LoD_{95\%}$ of 80 mm. (c and d) As (a), but showing only areas where the original point clouds were detected to be significantly different by M3C2 (c) or M3C2-PM (d).

Figure 13. Schematic illustration of factors in precision-based planning of UAV missions based on (a) photogrammetric considerations, or control (georeferencing) characteristics for (b) GCP-georeferenced and (c) directly georeferenced surveys. Triangles represent camera positions and orientations, above a grey-shaded topography. Ellipses indicate control measurements, either of GCPs or camera positions, with their relative size indicative of the relative precision magnitude.

References

Bláha M, Eisenbeiss H, Grimm D, Limpach P. 2011. Direct georeferencing of UAVs. International Archives of Photogrammetry and Remote Sensing and Spatial Information Sciences **XXXVIII-1/C22**: 131-136

Borradaile GJ. 2003. Statistics of Earth Science Data : their distribution in space, time, and orientation. Springer-Verlag Berlin: Heidelberg

Brasington J, Langham J, Rumsby B. 2003. Methodological sensitivity of morphometric estimates of coarse fluvial sediment transport. Geomorphology **53**: 299-316. DOI: 10.1016/S0169-555x902)00320-3

Cantón Y, Domingo F, Solé-Benet A, Puigdefábregas J. 2001. Hydrological and erosion response of a badlands system in semiarid SE Spain. Journal of Hydrology **252**: 65-84. DOI: 10.1016/s0022-1694(01)00450-4

Carbonneau PE, Dietrich JT. 2016. Cost-Effective non-metric photogrammetry from consumer-grade sUAS: Implications for direct georeferencing of structure from motion photogrammetry. Earth Surface Processes and Landforms: in press. DOI: 10.1002/esp.4012

Casella E, Rovere A, Pedroncini A, Mucerino L, Casella M, Cusati LA, Vacchi M, Ferrari M, Firpo M. 2014. Study of wave runup using numerical models and low-altitude aerial photogrammetry: A tool for coastal management. Estuarine Coastal and Shelf Science **149**: 160-167. DOI: 10.1016/j.ecss.2014.08.012

Castillo C, Pérez R, James MR, Quinton NJ, Taguas EV, Gómez JA. 2012. Comparing the accuracy of several field methods for measuring gully erosion. Soil Science Society of America Journal **76**: 1319-1332. DOI: 10.2136/sssaj2011.0390

Chandler J. 1999. Effective application of automated digital photogrammetry for geomorphological research. Earth Surface Processes and Landforms **24**: 51-63

Chiang K-W, Tsai M-L, Chu D-H. 2012. The Development of an UAV borne direct georeferenced photogrammetric platform for ground control point free applications. Sensors **12**: 9161-9180. DOI: 10.3390/s120709161

Chu H-J, Chen R-A, Tseng Y-H, Wang C-K. 2014. Identifying LiDAR sample uncertainty on terrain features from DEM simulation. Geomorphology **204**: 325-333. DOI: 10.1016/j.geomorph.2013.08.016

Clarke TA, Fryer JG. 1998. The development of camera calibration methods and models. Photogrammetric Record **16**: 51-66. DOI: 10.1111/0031-868x.00113

Cooper MAR, Robson S. 1996. Theory of close range photgrammetry. In Close range photogrammetry and machine vision, Atkinson KB (ed). Whittles Publishing: Caithness; 9-51.

Cramer M, Stallmann D, Haala N. 2000. Direct georeferencing usin GPS/inertial exterior orientations for photogrammetric applications. International Archives of the Photogrammetry, Remote Sensing and Spatial Information Sciences **XXXIII, Part B3**: 198-205

Dietrich JT. 2016. Riverscape mapping with helicopter-based Structure-from-Motion photogrammetry. Geomorphology **252**: 144-157. DOI: 10.1016/j.geomorph.2015.05.008

Eling C, Wieland M, Hess C, Klingbeil L, Kuhlmann H. 2015. Development and evaluation of a UAV based mapping system for remote sensing and surveying applications. International Archives of Photogrammetry, Remote Sensing, and Spatial Information Sciences **XL-1/W4**: 233-239. DOI: 10.5194/isprsarchives-XL-1-W4-233-2015

Eltner A, Baumgart P, Maas HG, Faust D. 2015. Multi-temporal UAV data for automatic measurement of rill and interrill erosion on loess soil. Earth Surface Processes and Landforms **40**: 741-755. DOI: 10.1002/esp.3673

Eltner A, Kaiser A, Castillo C, Rock G, Neugirg F, Abellan A. 2016. Image-based surface reconstruction in geomorphometry - merits, limits and developments. Earth Surface Dynamics **4**: 359-389. DOI: 10.5194/esurf-4-359-2016

Förstner W, Wrobel B, Paderes F, Fraser CS, Dolloff J, Mikhail EM, Rajikietgumjorn W. 2013. Analytical photogrammetric operations. In Manual of Photogrammetry, McGlone JC (ed). American Society for Photogrammetry and Remote Sensing: Bethesda.

Förstner W, Wrobel BP. 2013. Mathematical concepts in photogrammetry. In Manual of photogrammetry, McGlone JC (ed). American Society for Photogrammetry and Remote Sensing: Bethesda.

Furukawa Y, Ponce J. 2007. Accurate, dense, and robust multi-view stereopsis. In *IEEE Conference on Computer Vision and Pattern Recognition (CVPR)*. DOI: 10.1109/CVPR.2007.383246

Gabrlik P. 2015. The use of direct georeferencing in aerial photogrammetry with micro UAV. IFAC-PapersOnLine **48**: 380–385

Gomez-Gutierrez A, Schnabel S, Berenguer-Sempere F, Lavado-Contador F, Rubio-Delgado J. 2014. Using 3D photo-reconstruction methods to estimate gully headcut erosion. Catena **120**: 91-101. DOI: 10.1016/j.catena.2014.04.004

Gonga-Saholiariliva N, Gunnell Y, Petit C, Mering C. 2011. Techniques for quantifying the accuracy of gridded elevation models and for mapping uncertainty in digital terrain analysis. Progress In Physical Geography **35**: 739-764. DOI: 10.1177/0309133311409086

Granshaw SI. 1980. Bundle adjustment methods in engineering photogrammetry. Photogrammetric Record **10**: 181-207

Hirschmuller H. 2008. Stereo processing by semiglobal matching and mutual information. IEEE Transactions on Pattern Analysis and Machine Intelligence **30**: 328-341. DOI: 10.1109/Tpami.2007.1166

Hugenholtz C, Brown O, Walker J, Barchyn T, Nesbit P, Kurcharczyk M, Myshak S. 2016. Spatial accuracy of UAV-derived orthoimagery and topography: Comparing photogrammetric models processed with direct geo-referencing and ground control points. Geomatica **70**: 21-30. DOI: 10.5623/cig2016-102

James MR, Robson S. 2012. Straightforward reconstruction of 3D surfaces and topography with a camera: Accuracy and geoscience application. Journal of Geophysical Research **117**: F03017. DOI: 10.1029/2011JF002289

James MR, Robson S. 2014a. Mitigating systematic error in topographic models derived from UAV and ground-based image networks. Earth Surface Processes and Landforms **39**: 1413-1420. DOI: 10.1002/esp.3609

James MR, Robson S. 2014b. Sequential digital elevation models of active lava flows from ground-based stereo time-lapse imagery. ISPRS Journal of Photogrammetry and Remote Sensing **97**: 160-170. DOI: 10.1016/j.isprsjprs.2014.08.011

James MR, Robson S, d'Oleire-Oltmanns S, Niethammer U. 2017. Optimising UAV topographic surveys processed with structure-from-motion: Ground control quality, quantity and bundle adjustment. Geomorphology **280**: 51–66. DOI: 10.1016/j.geomorph.2016.11.021

James MR, Varley N. 2012. Identification of structural controls in an active lava dome with high resolution DEMs: Volcán de Colima, Mexico. Geophysical Research Letters **39**: L22303. DOI: 10.1029/2012GL054245

Javernick L, Hicks DM, Measures R, Caruso B, Brasington J. 2016. Numerical modelling of braided rivers with structure-from-motion-derived terrain models. River Research and Applications **32**: 1071-1081. DOI: 10.1002/rra.2918

Krauss K. 1993. Photogrammetry, Vol. 1, Fundamentals and Standard Processes. Dümmlers

Lague D, Brodu N, Leroux J. 2013. Accurate 3D comparison of complex topography with terrestrial laser scanner: Application to the Rangitikei canyon (N-Z). ISPRS Journal of Photogrammetry and Remote Sensing **82**: 10-26. DOI: 10.1016/j.isprsjprs.2013.04.009

Lallias-Tacon S, Liebault F, Piegay H. 2014. Step by step error assessment in braided river sediment budget using airborne LiDAR data. Geomorphology **214**: 307-323. DOI: 10.1016/j.geomorph.2014.02.014

Lane SN, James TD, Crowell MD. 2000. Application of digital photogrammetry to complex topography for geomorphological research. Photogrammetric Record **16**: 793-821. DOI: 10.1111/0031-868x.00152

Lane SN, Westaway RM, Hicks DM. 2003. Estimation of erosion and deposition volumes in a large, gravel-bed, braided river using synoptic remote sensing. Earth Surface Processes and Landforms **28**: 249-271. DOI: 10.1002/esp.483

Lucieer A, de Jong SM, Turner D. 2014. Mapping landslide displacements using Structure from Motion (SfM) and image correlation of multi-temporal UAV photography. Progress In Physical Geography **38**: 97-116. DOI: 10.1177/0309133313515293

Luhmann T, Robson S, Kyle S, Harley I. 2006. Close range photogrammetry: Principles, methods and applications. Whittles, Caitness

Mian O, Lutes J, Lipa G, Hutton JJ, Gavelle E, Borghini S. 2015. Direct georeferencing on small unmanned aerial platforms for improved reliability and accuracy of mapping without the need for ground control points. International Archives of Photogrammetry, Remote Sensing, and Spatial Information Sciences **XL-1/W4**: 397-402. DOI: 10.5194/isprsarchives-XL-1-W4-397-2015

Milan DJ, Heritage GL, Hetherington D. 2007. Application of a 3D laser scanner in the assessment of erosion and deposition volumes and channel change in a proglacial river. Earth Surface Processes and Landforms **32**: 1657-1674. DOI: 10.1002/esp.1592

Milan DJ, Heritage GL, Large ARG, Fuller IC. 2011. Filtering spatial error from DEMs: Implications for morphological change estimation. Geomorphology **125**: 160-171. DOI: 10.1016/j.geomorph.2010.09.012

Mosbrucker AR, Major JJ, Spicer KR, Pitlick J. 2017. Camera system considerations for geomorphic applications of SfM photogrammetry. Earth Surface Processes and Landforms. In press. DOI: 10.1002/esp.4066

Nadal-Romero E, Martinez-Murillo JF, Vanmaercke M, Poesen J. 2011. Scale-dependency of sediment yield from badland areas in Mediterranean environments. Progress In Physical Geography **35**: 297-332. DOI: 10.1177/0309133311400330

Nolan M, DesLauriers K. 2016. Which are the highest peaks in the US Arctic? Fodar settles the debate. The Cryosphere **10**: 1245-1254

Nolan M, Larsen C, Sturm M. 2015. Mapping snow depth from manned aircraft on landscape scales at centimeter resolution using structure-from-motion photogrammetry. Cryosphere **9**: 1445-1463. DOI: 10.5194/tc-9-1445-2015

Oksanen J, Sarjakoski T. 2006. Uncovering the statistical and spatial characteristics of fine toposcale DEM error. International Journal of Geographical Information Science **20**: 345-369. DOI: 10.1080/13658810500433891

Pfeifer N, Glira P, Briese C. 2012. Direct georeferencing with on board navigation components of light weight UAV platforms. International Archives of the Photogrammetry, Remote Sensing and Spatial Information Sciences **XXXIX-B7**: 487-492

Rehak M, Mabillard R, Skaloud J. 2013. A micro-UAV with the capability of direct georeferencing. International Archives of the Photogrammetry, Remote Sensing and Spatial Information Sciences **XL-1/W2**: 317-323

Ryan JC, Hubbard AL, Box JE, Todd J, Christoffersen P, Carr JR, Holt TO, Snooke N. 2015. UAV photogrammetry and structure from motion to assess calving dynamics at Store Glacier, a large outlet draining the Greenland ice sheet. Cryosphere **9**: 1-11. DOI: 10.5194/tc-9-1-2015

Smith MW, Quincey DJ, Dixon T, Bingham RG, Carrivick JL, Irvine-Fynn TDL, Rippin DM. 2016. Aerodynamic roughness of glacial ice surfaces derived from high-resolution topographic data. Journal of Geophysical Research-Earth Surface **121**: 748-766. DOI: 10.1002/2015jf003759

Smith MW, Vericat D. 2015. From experimental plots to experimental landscapes: topography, erosion and deposition in sub-humid badlands from Structure-from-Motion photogrammetry. Earth Surface Processes and Landforms **40**: 1656-1671. DOI: 10.1002/esp.3747

Tang RF, Fritsch D. 2013. Correlation Analysis of Camera Self-Calibration in Close Range Photogrammetry. Photogrammetric Record **28**: 86-95. DOI: 10.1111/phor.12009

Turner D, Lucieer A, Wallace L. 2014. Direct georeferencing of ultrahigh-resolution UAV imagery. IEEE Transactions on Geoscience and Remote Sensing **52**: 2738-2745. DOI: 10.1109/Tgrs.2013.2265295

Wackrow R, Chandler JH. 2011. Minimising systematic error surfaces in digital elevation models using oblique convergent imagery. Photogrammetric Record **26**: 16-31. DOI: 10.1111/j.1477-9730.2011.00623.x

Wackrow R, Chandler JH, Bryan P. 2007. Geometric consistency and stability of consumer-grade digital cameras for accurate spatial measurement. The Photogrammetric Record **22**: 121-134

Wechsler SP. 2007. Uncertainties associated with digital elevation models for hydrologic applications: a review. Hydrology and Earth System Sciences **11**: 1481-1500

Weng QH. 2002. Quantifying uncertainty of digital elevation models derived from topographic maps. In Advances in Spatial Data Handling, Richardson D, van Oosterom P (eds). Springer Berlin Heidelberg; 403-418.

Westoby MJ, Brasington J, Glasser NF, Hambrey MJ, Reynolds JM, Hassan MAAM, Lowe A. 2015. Numerical modelling of glacial lake outburst floods using physically based dam-breach models. Earth Surface Dynamics **3**: 171-199. DOI: 10.5194/esurf-3-171-2015

Wheaton JM, Brasington J, Darby SE, Sear DA. 2010. Accounting for uncertainty in DEMs from repeat topographic surveys: improved sediment budgets. Earth Surface Processes and Landforms **35**: 136-156. DOI: 10.1002/esp.1886

Woodget AS, Carbonneau PE, Visser F, Maddock IP. 2015. Quantifying submerged fluvial topography using hyperspatial resolution UAS imagery and structure from motion photogrammetry. Earth Surface Processes and Landforms **40**: 47-64. DOI: 10.1002/esp.3613

Tables

Table 1. Characteristics of the simulated surveys shown in Figure 2.

Survey detail			Values and characteristics
Camera		Principal dist.	50 mm
		Image size	4000 × 3000 pix. (pixel pitch 5 μm)
Flight plan (Figure 2)		Altitude	50 m
		Ground pix. size	12·5 mm (nominal)
		Image overlap	60% forward 30% sidelap (within each parallel set)
	Network geometry	**Weak**	80 images, collected from two sets of parallel flight lines, oriented at 20° (Figure 6/7 a, c)
		Strong	An additional 18 images, in two gently banked turns (Figure 6/7 b, d)

Georeferencing scenarios		Control survey precision (GCPs or camera pos.) horizontal	Control survey precision (GCPs or camera pos.) vertical	Image measurement precision (pix) GCPs	Image measurement precision (pix) Tie points
Using GCPs	**Strong** (Fig. 6a, b)	10 mm	20 mm	0·1	1·0
	Weak (Fig. 6c, d)	50 mm	100 mm	1·0	0·1
Direct georeferencing	**Strong** (Fig. 7a, b)	20 mm	40 mm	-	0·5
	Weak (Fig. 7c, d)	2 m	4 m	-	0·5

Table 2. Characteristics of the 2014 and 2015 badlands surveys.

	2014	2015
Camera		
Model	Nikon D3100	Nikon D75
Focal length (35-mm equiv.; mm)	28	28
Image size (pix)	4608 × 3584	6016 × 4016
Pixel pitch (µm)	5·0	6·0
Survey		
Overflight design	7–10 oblique overpasses, mutually inclined, nominal altitude of 50 m (Figure 5d)	
GCP coordination	dGPS, absolute quality available per-point, means: *XY*: 14 mm, Z: 26 mm	total station, 3-D quality relative to instrument[a]: *XY*: 10 mm, Z: 5 mm
Processing		
Number of images processed	104	99
GCPs (as control, [as check] pts.)	19 [7]	20 [7]
GCP image precision (pix)	0·50	1·55
Tie point image precision (pix)	0·89	1·26
RMS discrepancies on GCPs :		
Control points (*X*, *Y*, *Z*; mm)	55·6, 42·4, 36·8	13·8 14·1 14·3
Check points (*X*, *Y*, *Z*; mm)	47·5, 54·8, 24·4	5·7 13·4 11·9

[a] Measurement precision reported by the instrument was ~1 mm, values given here account for additional uncertainty due to locating the prism over the GCP.

Table 3. Parameters and survey precision characteristics for the 2014 badlands survey, processed with GCPs as control.

Parameter or characteristic		PhotoScan[a]	VMS[b]
Camera model (*Model A*)		*Value ± precision*	
Principal distance (P.D.; pix)		3786·42 ± 0·16	3786·40 ± 0·12
Principal point coords. (pix)	CC*x*	2295·45 ± 0·08	2296·06 ± 0·04
	CC*y*	1570·16 ± 0·13	1569·72 ± 0·08
Radial distortion	K_1	$-9{\cdot}2484\times10^{-2} \pm 8{\cdot}52\times10^{-5}$	$-9{\cdot}2265\times10^{-2} \pm 7{\cdot}43\times10^{-5}$
	K_2	$3{\cdot}5033\times10^{-2} \pm 3{\cdot}57\times10^{-4}$	$3{\cdot}4263\times10^{-2} \pm 3{\cdot}09\times10^{-4}$
	K_3	$3{\cdot}1925\times10^{-3} \pm 4{\cdot}51\times10^{-4}$	$4{\cdot}3945\times10^{-3} \pm 3{\cdot}62\times10^{-4}$
Camera orientations		*Mean precision across all cameras*	
Position (*X*, *Y*, *Z*; mm)		16·4, 26·2, 30·5	14·4, 22·3, 26·7
Rotation (roll, pitch, yaw; mdeg.)		21·1, 9·0, 9·1	18·2, 8·0, 8·2
Survey overall georeferencing		*Precision*	
Translation (*X*, *Y*, *Z*; mm)		2·6, 2·4, 5·6	n./a.
Slope (angles to *X*, *Y*, *Z* axes; mdeg.)		7·5, 17·4, 0·3	n./a.
Scale (%)		0·0072	n./a.
3-D topographic point coordinates		*Mean precision across all points in region of interest*	
Precision (*X*, *Y*, *Z*; mm)		18·6, 14·5, 26·1	18·2, 14·2, 25·2
Shape only[c] (*X*, *Y*, *Z*; mm)		18·3, 13·9, 23·3	17·9, 13·8, 23·0
		Dimensionless relative precision ratios (full survey)	
Mean precision : max. survey extent		1 : 29,600	1 : 29,600
Mean precision : mean obs. distance		1 : 4,100	1 : 4,100
Mean precision in pixels (*XY*, *Z*; pix.)		1·3, 1·1	1·2, 1·1

[a] Precision values determined using Monte Carlo analysis.

[b] VMS used only to run a bundle adjustment on the image network derived by PhotoScan. Camera parameter values are given in the convention used in PhotoScan.

[c] 'Shape only' precision is determined after accounting for uncertainty in overall georeferencing.

Table 4. Parameter correlations for the two camera models tested for the 2014 badlands survey. *CCx* and *CCy* are the principal point coordinates, *P.D.* is the principal distance (focal length), $K_{1\text{-}3}$ are radial distortion parameters and $P_{1,\ 2}$ are tangential distortion parameters. Underscores highlight correlation magnitudes that exceed 0·10 (except those from self-correlation).

	Camera model A						Camera model B							
	CCx	*CCy*	*P.D.*	K_1	K_2	K_3	*CCx*	*CCy*	*P.D.*	K_1	K_2	K_3	P_1	P_2
CCx	1·00						1·00							
CCy	-0·05	1·00					-0·05	1·00						
P.D.	-0·09	-0·62	1·00				-0·41	-0·17	1·00					
K_1	-0·03	-0·09	-0·03	1·00			-0·04	0·00	-0·10	1·00				
K_2	0·03	0·08	0·10	-0·96	1·00		0·10	0·01	0·09	-0·96	1·00			
K_3	-0·03	-0·09	-0·07	0·91	-0·98	1·00	-0·07	-0·02	-0·09	0·91	-0·98	1·00		
P_1							0·27	0·19	0·45	-0·06	0·04	-0·03	1·00	
P_2							-0·04	-0·89	0·18	0·02	-0·01	0·00	0·14	1·00

Table 5. Sediment budget between 2014 and 2015, calculated using different methods to determine the regions of detectable change. Average topographic change was determined using a catchment of 4710 m^2 and a 1·12 a inter-survey interval.

Calculation method used	Total erosion (m^3)	Total deposition (m^3)	Net (m^3)	Average topographic change (mm a^{-1})
DoD	-210·49	17·87	-192·61	-36·5
DoD $LoD_{95\%}$	-142·54	8·76	-133·78	-25·4
M3C2	-18·89	0·21	-18·68	-3·5
M3C2-PM	-98·65	2·82	-95·83	-18·2

Figure 01

a

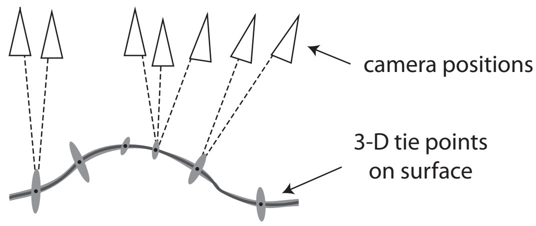

No georeferencing
surface model has shape, but arbitrary scale, translation and rotation with respect to a geographic coordinate system

b

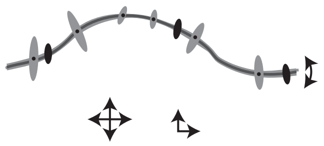

'Strong' georeferencing
precision limited by photogrammetric considerations; small uncertainties in model scale, translation and rotation

c

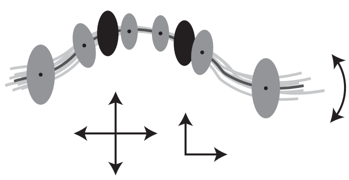

'Weak' georeferencing
precision limited by georeferencing considerations; large uncertainties in model scale, translation and rotation

Figure 02

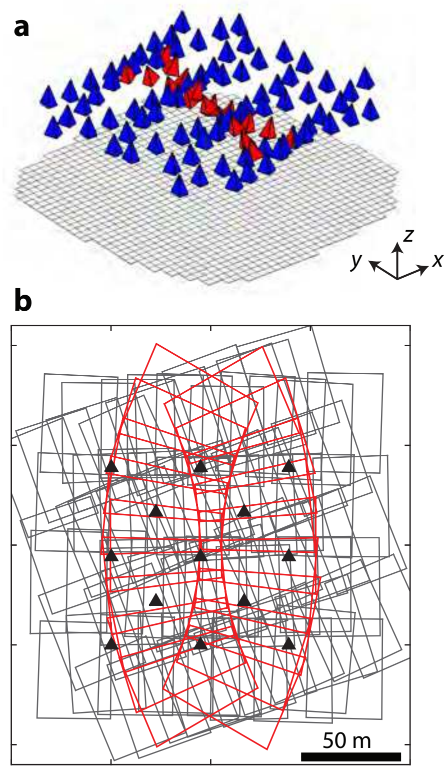

Figure 03

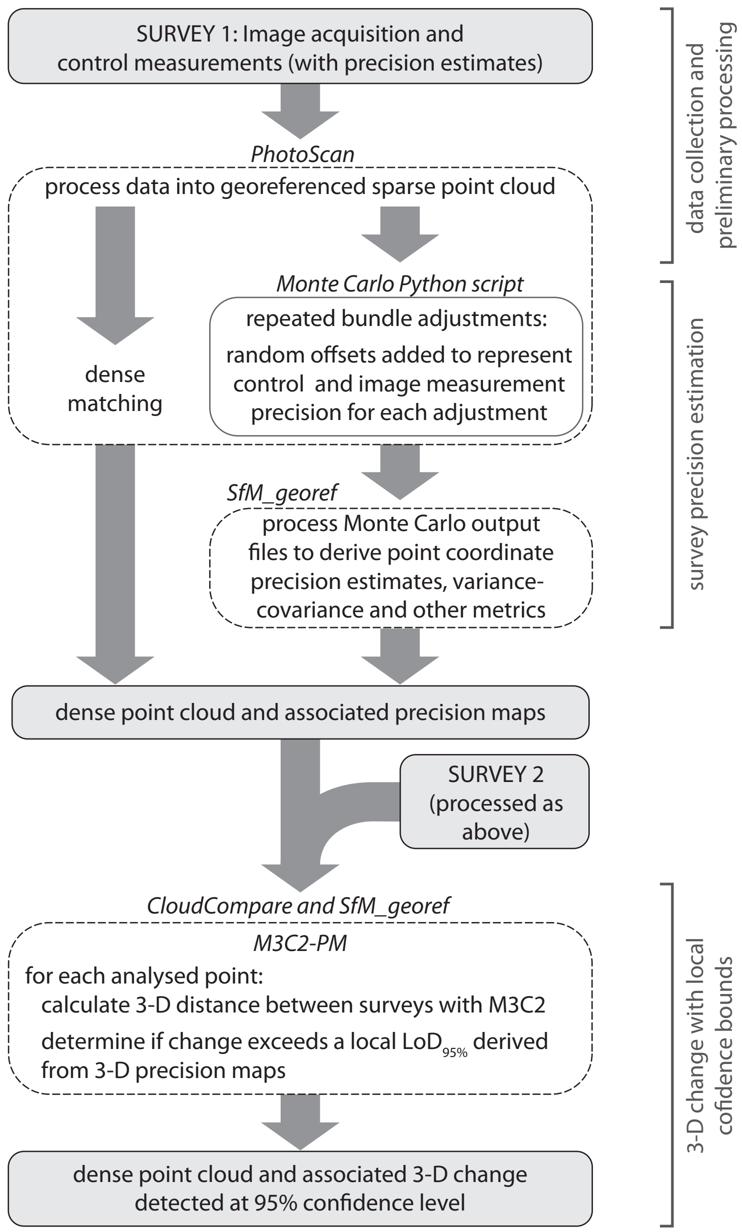

SURVEY 1: Image acquisition and control measurements (with precision estimates)
PhotoScan
process data into georeferenced sparse point cloud
Monte Carlo Python script
repeated bundle adjustments:
random offsets added to represent control and image measurement precision for each adjustment
dense matching
SfM_georef
process Monte Carlo output files to derive point coordinate precision estimates, variance-covariance and other metrics
dense point cloud and associated precision maps
SURVEY 2 (processed as above)
CloudCompare and SfM_georef
M3C2-PM
for each analysed point:
calculate 3-D distance between surveys with M3C2
determine if change exceeds a local LoD95% derived from 3-D precision maps
dense point cloud and associated 3-D change detected at 95% confidence level
data collection and preliminary processing
survey precision estimation
3-D change with local cofidence bounds

Figure 04

Step 1 (M3C2): Calculation of normal **N** at a scale D around the core point i in cloud S_1.

Step 2 (M3C2): Average distance between the two cloud measured along **N** between mean points i_1 and i_2, derived at a scale d.

Step 3: Position uncertainty for i_1 and i_2 ascertained from precision maps and used to determine distance uncertainty in direction **N**.

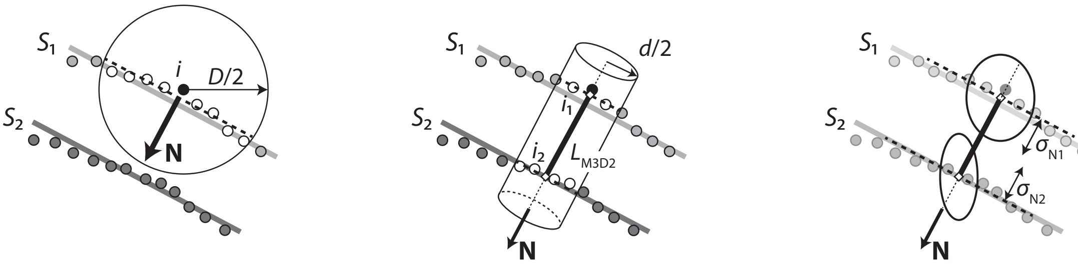

Figure 05

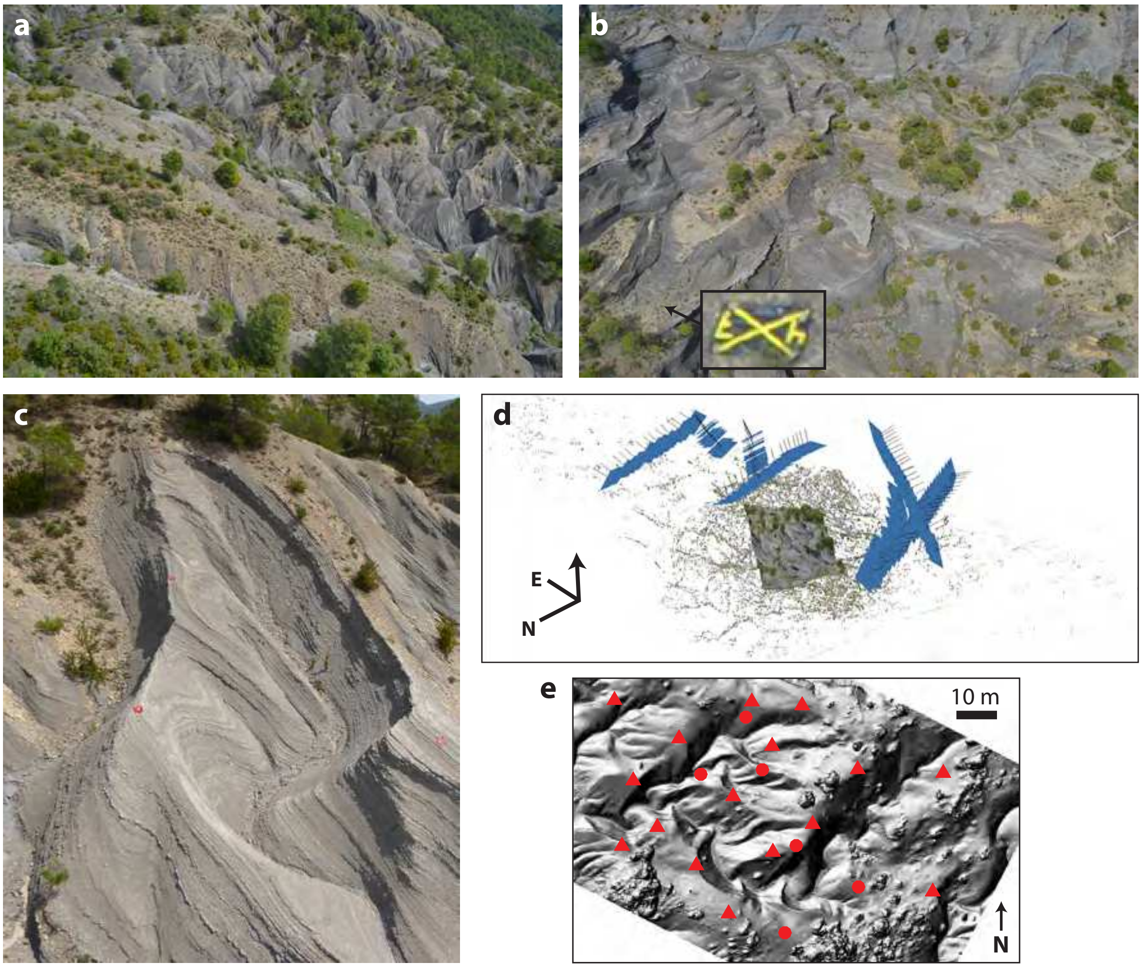

Figure 06

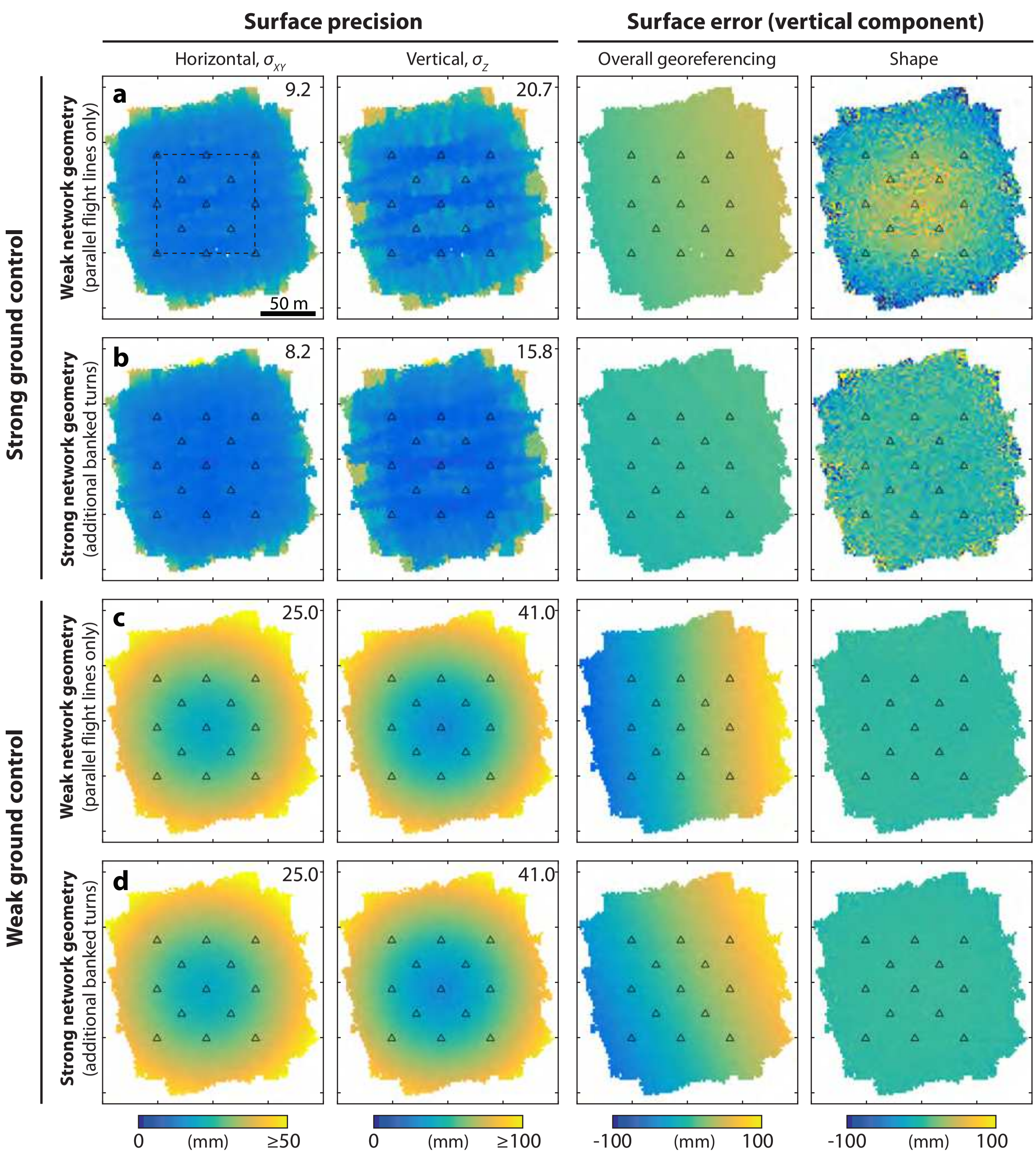
Surface precision
Surface error (vertical component)
Horizontal, σ_{XY}
Vertical, σ_Z
Overall georeferencing
Shape
Strong ground control
Weak ground control
Weak network geometry
(parallel flight lines only)
Strong network geometry
(additional banked turns)
a
b
c
d
9.2
20.7
8.2
15.8
25.0
41.0
25.0
41.0
50 m
0
(mm)
≥50
0
(mm)
≥100
-100
(mm)
100
-100
(mm)
100

Figure 07

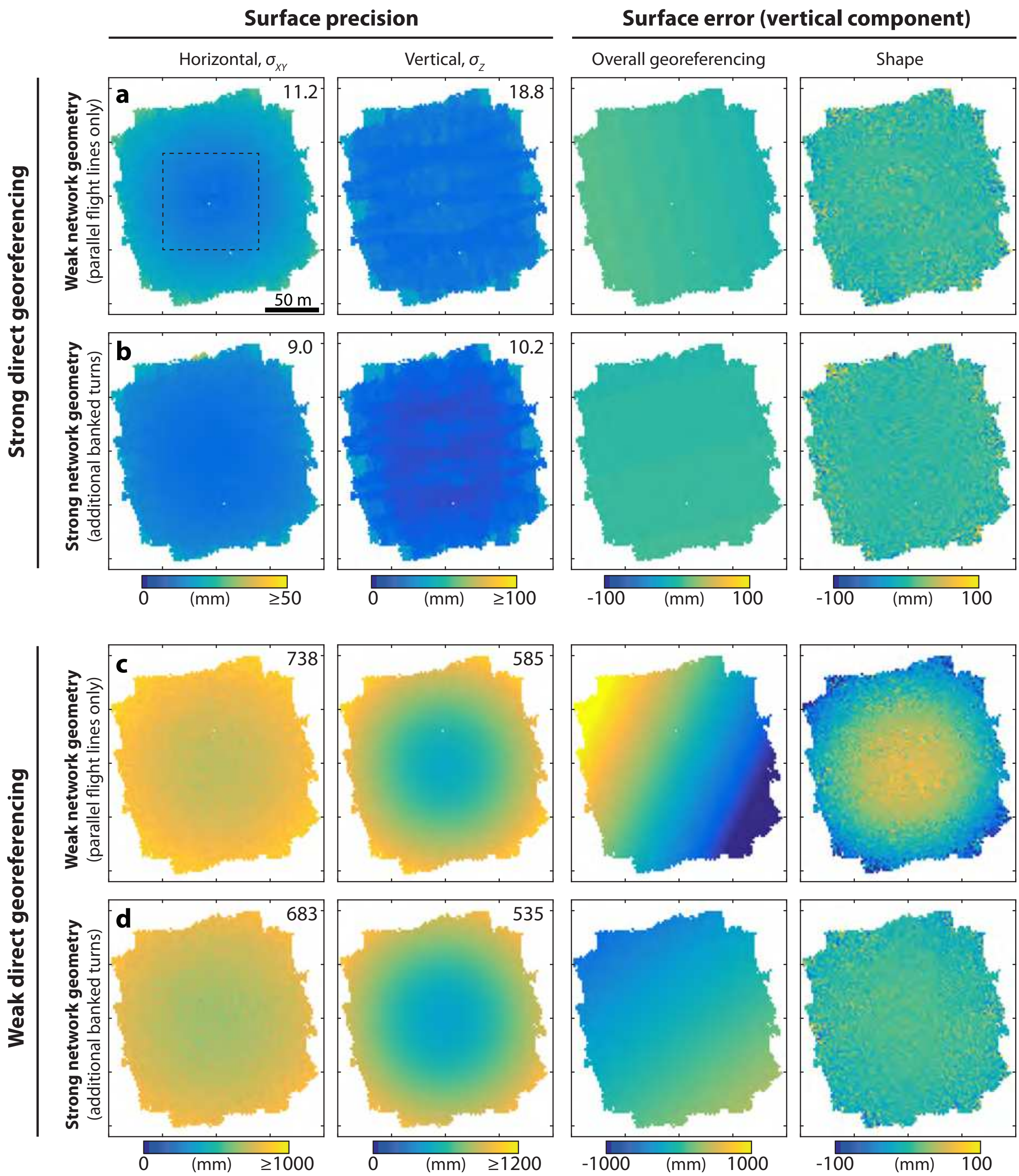

Surface precision
Surface error (vertical component)
Horizontal, σ_{XY}
Vertical, σ_Z
Overall georeferencing
Shape
Strong direct georeferencing
Weak network geometry
(parallel flight lines only)
Strong network geometry
(additional banked turns)
a
11.2
18.8
50 m
b
9.0
10.2
0
(mm)
≥50
0
(mm)
≥100
-100
(mm)
100
-100
(mm)
100
Weak direct georeferencing
Weak network geometry
(parallel flight lines only)
Strong network geometry
(additional banked turns)
c
738
585
d
683
535
0
(mm)
≥1000
0
(mm)
≥1200
-1000
(mm)
1000
-100
(mm)
100

Figure 08

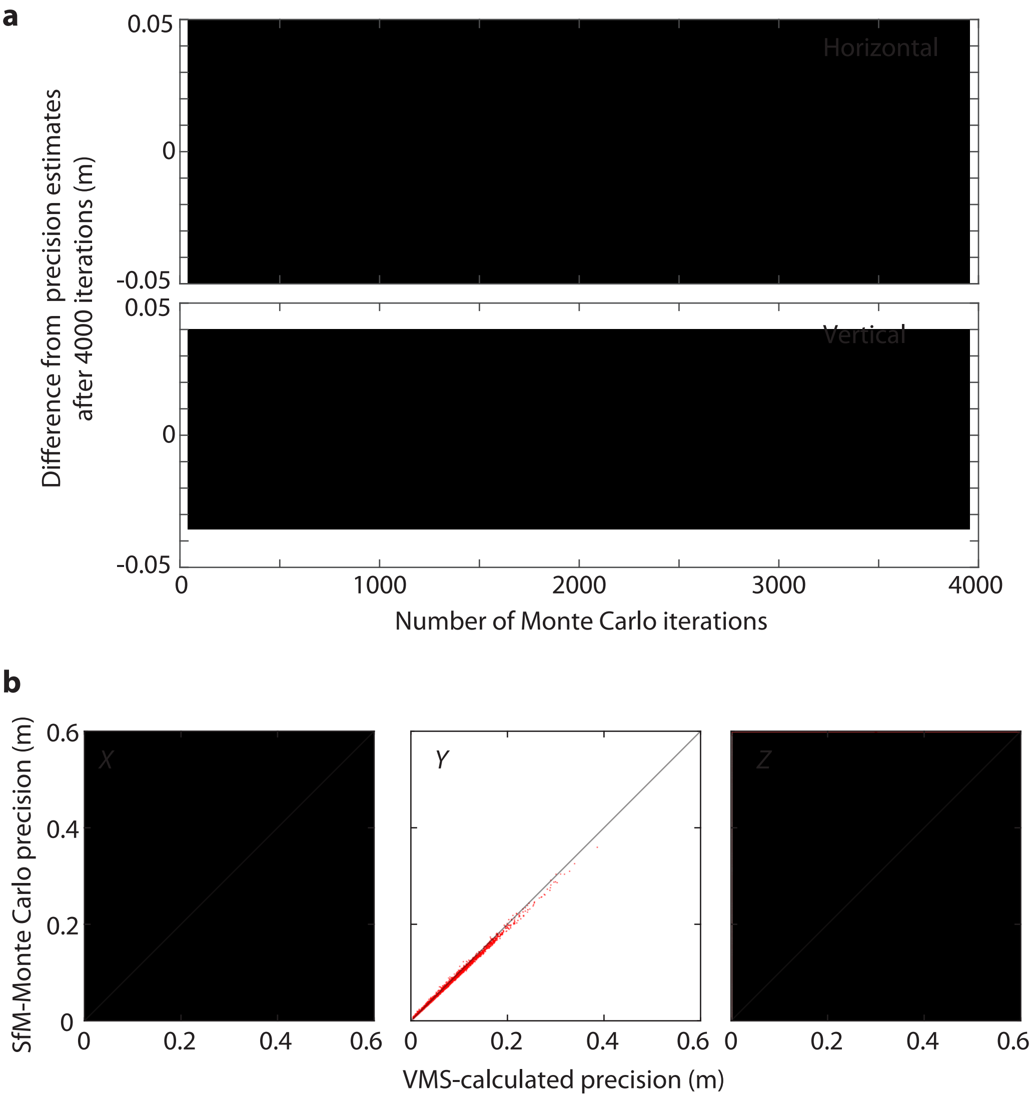
a
Difference from precision estimates after 4000 iterations (m)
0.05
0
-0.05
Horizontal
Vertical
0
1000
2000
3000
4000
Number of Monte Carlo iterations
b
SfM-Monte Carlo precision (m)
0.6
0.4
0.2
0
X
Y
Z
VMS-calculated precision (m)

Figure 09

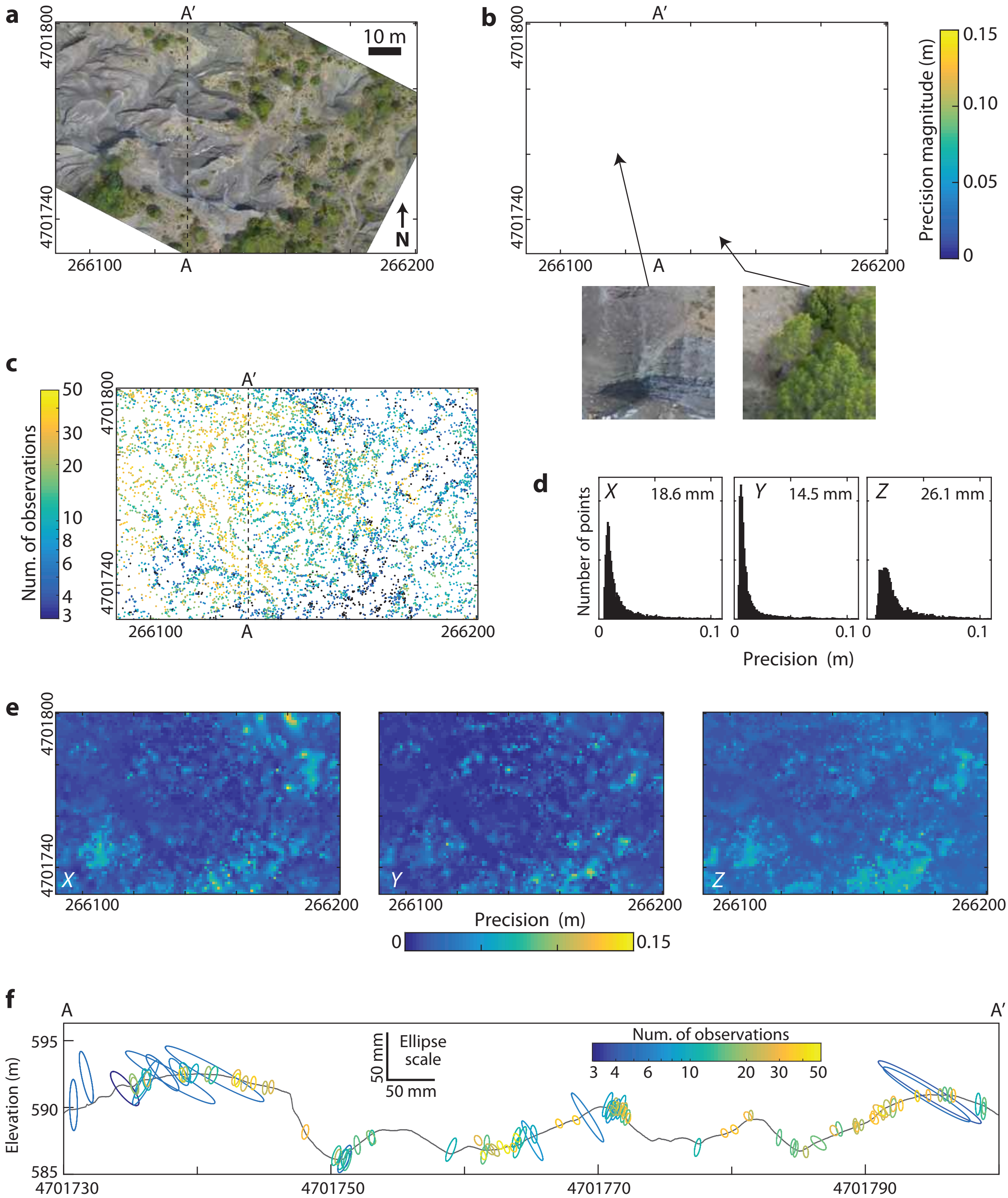

a
b
c
d
e
f
A′
A
10 m
N
4701800
4701740
266100
266200
Precision magnitude (m)
0.15
0.10
0.05
0
Num. of observations
50
30
20
10
8
6
4
3
Number of points
X 18.6 mm
Y 14.5 mm
Z 26.1 mm
0.1
Precision (m)
X
Y
Z
Elevation (m)
595
590
585
4701730
4701750
4701770
4701790
50 mm
Ellipse scale

Figure 10

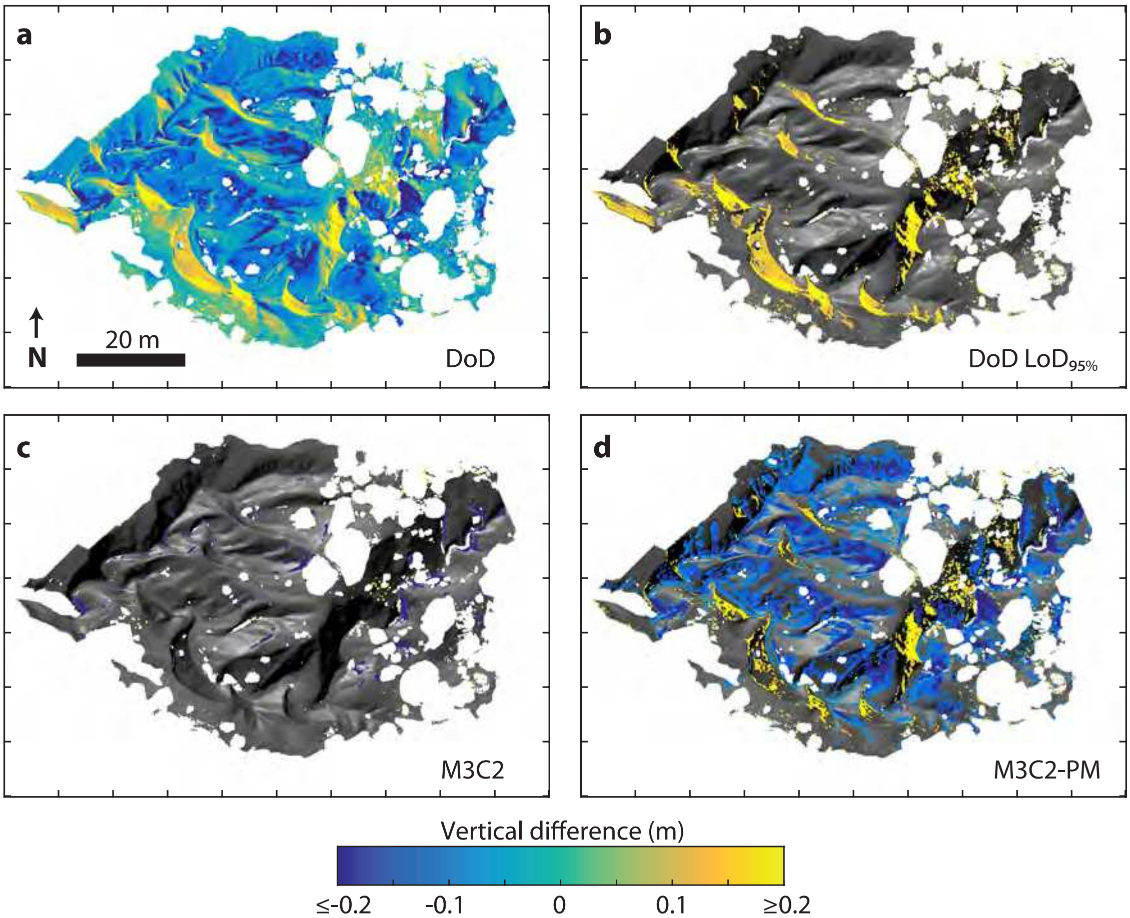

a
b
c
d
N
20 m
DoD
DoD $LoD_{95\%}$
M3C2
M3C2-PM
Vertical difference (m)
≤-0.2
-0.1
0
0.1
≥0.2

Figure 11

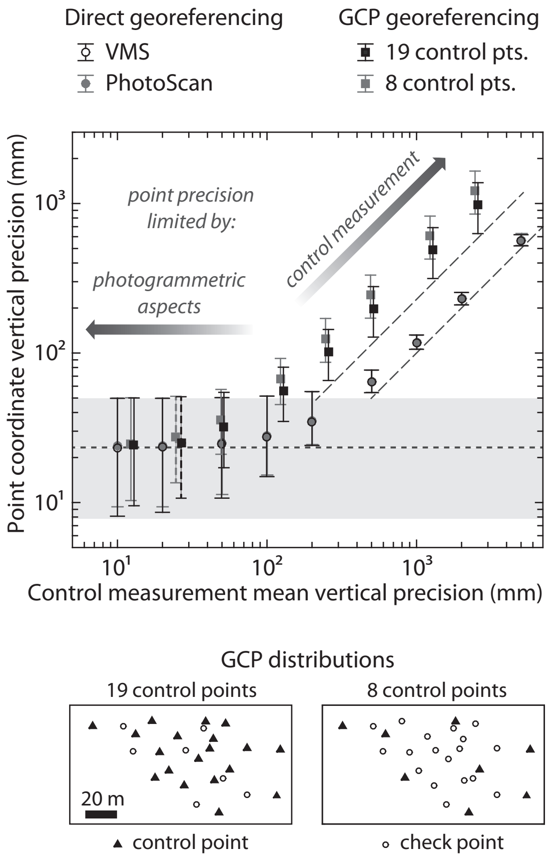

Direct georeferencing
VMS
PhotoScan
GCP georeferencing
19 control pts.
8 control pts.
point precision
limited by:
photogrammetric
aspects
control measurement
Point coordinate vertical precision (mm)
10^3
10^2
10^1
10^1
10^2
10^3
Control measurement mean vertical precision (mm)
GCP distributions
19 control points
8 control points
20 m
control point
check point

Figure 12

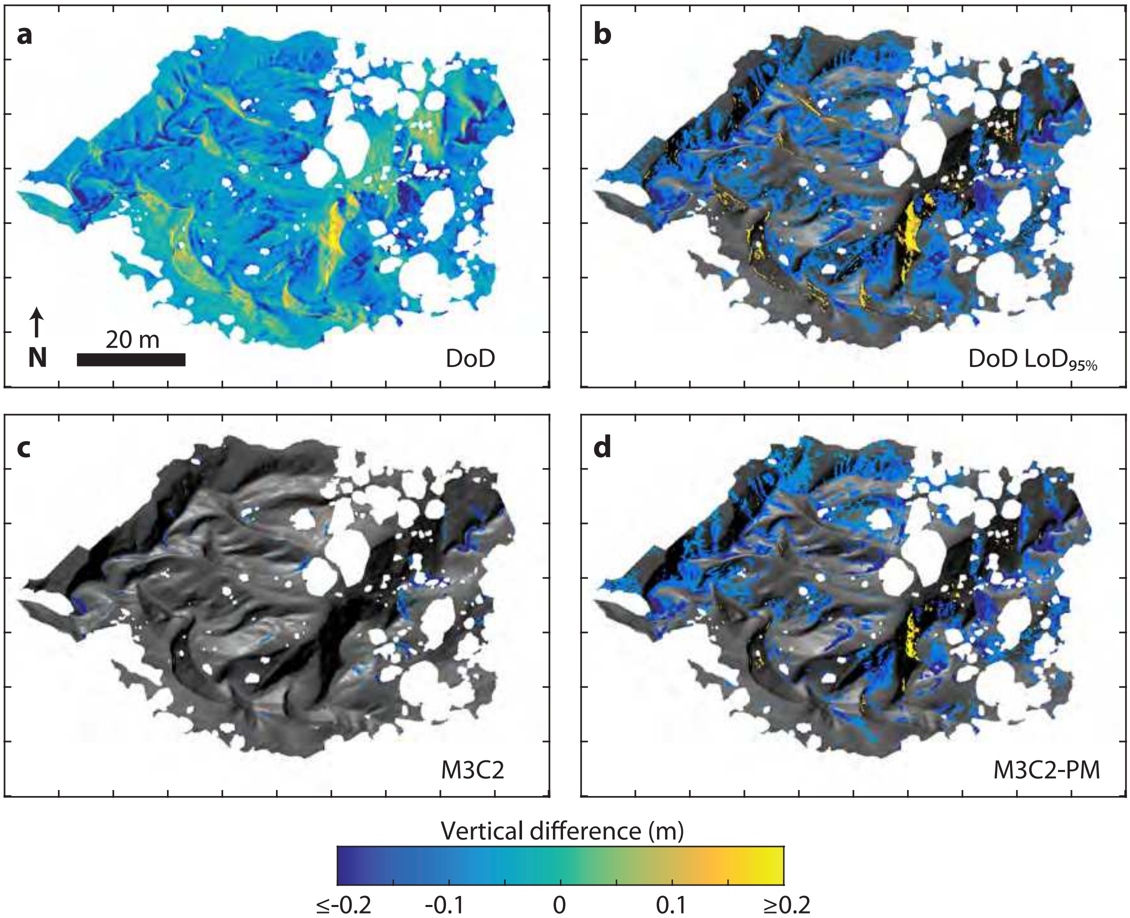

a
b
20 m
N
DoD
DoD LoD95%
c
d
M3C2
M3C2-PM
Vertical difference (m)
≤-0.2
-0.1
0
0.1
≥0.2

Figure 13

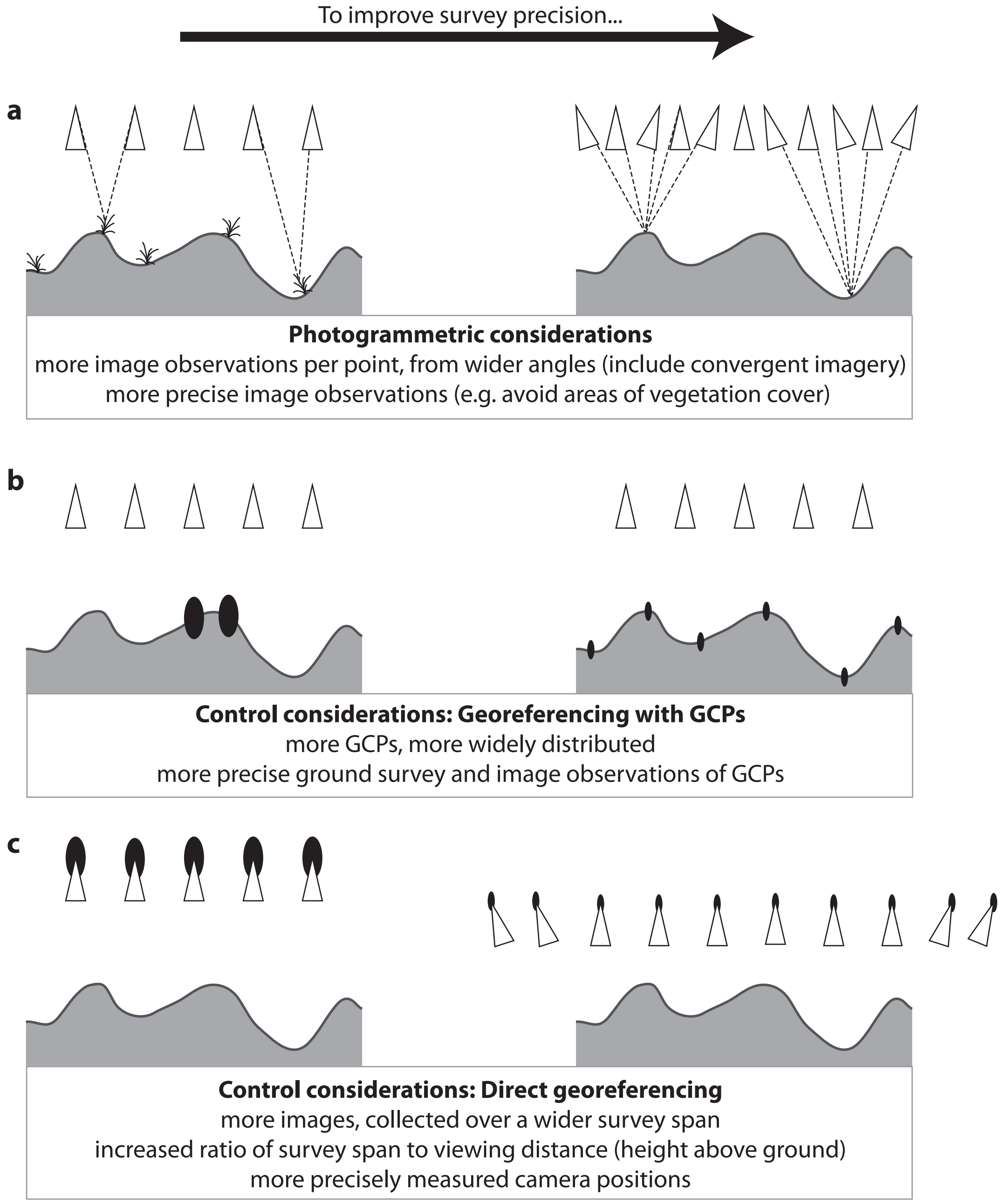

To improve survey precision...
a
Photogrammetric considerations
more image observations per point, from wider angles (include convergent imagery)
more precise image observations (e.g. avoid areas of vegetation cover)
b
Control considerations: Georeferencing with GCPs
more GCPs, more widely distributed
more precise ground survey and image observations of GCPs
c
Control considerations: Direct georeferencing
more images, collected over a wider survey span
increased ratio of survey span to viewing distance (height above ground)
more precisely measured camera positions